

A new determination of the primordial He abundance using the He I $\lambda 10830\text{\AA}$ emission line: cosmological implications

Y. I. Izotov¹, T. X. Thuan² and N. G. Guseva¹

¹*Main Astronomical Observatory, Ukrainian National Academy of Sciences, Zabolotnoho 27, Kyiv 03680, Ukraine*

²*Astronomy Department, University of Virginia, P.O. Box 400325, Charlottesville, VA 22904, USA*

Accepted 1988 December 15. Received 1988 December 14; in original form 1988 October 11

ABSTRACT

We present near-infrared spectroscopic observations of the high-intensity He I $\lambda 10830\text{\AA}$ emission line in 45 low-metallicity H II regions. We combined these NIR data with spectroscopic data in the optical range to derive the primordial He abundance. The use of the He I $\lambda 10830\text{\AA}$ line, the intensity of which is very sensitive to the density of the H II region, greatly improves the determination of the physical conditions in the He⁺ zone. This results in a considerably tighter $Y - \text{O}/\text{H}$ linear regression compared to all previous studies. We extracted a final sample of 28 H II regions with H β equivalent width $\text{EW}(\text{H}\beta) \geq 150\text{\AA}$, excitation parameter $\text{O}^{2+}/\text{O} \geq 0.8$, and with helium mass fraction Y derived with an accuracy better than 3%. With this final sample we derived a primordial ⁴He mass fraction $Y_p = 0.2551 \pm 0.0022$. The derived value of Y_p is higher than the one predicted by the standard big bang nucleosynthesis (SBBN) model. Using our derived Y_p together with $\text{D}/\text{H} = (2.53 \pm 0.04) \times 10^{-5}$, and the χ^2 technique, we found that the best agreement between these light element abundances is achieved in a cosmological model with a baryon mass density $\Omega_b h^2 = 0.0240 \pm 0.0017$ (68% CL), ± 0.0028 (95.4% CL), ± 0.0034 (99% CL) and an effective number of neutrino species $N_{\text{eff}} = 3.58 \pm 0.25$ (68% CL), ± 0.40 (95.4% CL), ± 0.50 (99% CL). A non-standard value of N_{eff} is preferred at the 99% CL, implying the possible existence of additional types of neutrino species.

Key words: galaxies: abundances — galaxies: irregular — galaxies: ISM — cosmology: cosmological parameters.

1 INTRODUCTION

In the standard theory of big bang nucleosynthesis (SBBN), given the number of light neutrino species, the abundances of light elements D, ³He, ⁴He (hereafter He) and ⁷Li depend only on one cosmological parameter, the baryon-to-photon number ratio η , which is related to the baryon density parameter Ω_b , the present ratio of the baryon mass density to the critical density of the Universe, by the expression $10^{10} \eta = 273.9 \Omega_b h^2$, where $h = H_0/100 \text{ km s}^{-1} \text{ Mpc}^{-1}$ and H_0 is the present value of the Hubble parameter (Steigman 2005, 2012).

Because of the strong dependence of the D/H abundance ratio on $\Omega_b h^2$ while the He mass fraction depends only logarithmically on the baryon density, deuterium is the light element of choice for determining the baryon mass fraction. Its abundance can accurately be measured in high-redshift low-metallicity QSO Ly α absorption systems. Although the data are still scarce – there are only ten absorp-

tion systems for which such a D/H measurement has been carried out (Pettini & Cooke 2012) – the measurements appear to converge to a mean primordial value $\text{D}/\text{H} \sim (2.5 - 2.9) \times 10^{-5}$, which corresponds to $\Omega_b h^2 \sim 0.0222 - 0.0223$ (Iocco et al. 2009; Noterdaeme et al. 2012; Pettini & Cooke 2012; Cooke et al. 2014). This estimate of $\Omega_b h^2$ is in excellent agreement with the value of 0.0221 - 0.0222 obtained from studies of the fluctuations of the cosmic microwave background (CMB) with *WMAP* and *Planck* (Keisler et al. 2011; Ade et al. 2013).

However, although deuterium is sufficient to derive the baryonic mass density from BBN, accurate measurements of the primordial He abundance Y_p are also needed as it plays a crucial role in determining cosmological parameters. First, it is needed to check the consistency of SBBN since this requires knowledge of the primordial abundances of at least two different relic elements. Second, while He is not a sensitive baryometer, its primordial abundance is much more sen-

sitive to a non-standard, early Universe expansion rate and thus provides stronger constraints on non-standard physics, as compared to other primordial light elements. Thus the primordial helium abundance can help constrain the effective number of neutrino species and hence place restrictions on the presence of any "dark radiation" component (e.g. "sterile" neutrinos, Di Valentino et al. 2013). It also put constraints on any possible lepton asymmetry (an excess of neutrinos over antineutrinos, or vice versa) that may exist (Steigman 2012).

To detect small deviations from SBBN and constrain cosmological parameters, the primordial He abundance Y_p has to be determined to a level of accuracy of better than one percent. The primordial abundance of He can in principle be derived accurately from observations of the helium and hydrogen emission lines from low-metallicity blue compact dwarf (BCD) galaxies, which have undergone little chemical evolution.

To attain the above accuracy, many conditions have to be met. In particular, the observational data should be of good quality and the observational sample should be large to reduce statistical uncertainties. The primary concern of our group over the last two decades has been to gather such good data for large galaxy samples. Izotov et al. (1994, 1997) and Izotov & Thuan (1998, 2004) have obtained high signal-to-noise spectra of a total of 86 low-metallicity extragalactic H II regions in 77 galaxies (Izotov & Thuan 2004), constituting the HeBCD sample. Later, Izotov et al. (2009, 2011) and Guseva et al. (2011) have used archival data to collect a sample of 75 Very Large Telescope (VLT) spectra of low-metallicity H II regions. Finally, 1442 high-quality spectra of low-metallicity H II regions have been extracted from the Sloan Digital Sky Survey (SDSS) Data Release 7 (DR7) (Abazajian et al. 2009). These were chosen to have the [O III] $\lambda 4363$ emission line measured with an accuracy better than 25%, and to have all strongest He I emission lines in the optical range, $\lambda 3889$, $\lambda 4471$, $\lambda 5876$, $\lambda 6678$, and $\lambda 7065$, measured with good accuracy. Because of the large sizes of these samples, it is now generally agreed that the accuracy of the determination of the primordial He abundance is limited at present more by systematic uncertainties and biases than by statistical errors.

There are many known effects that need to be corrected for to transform the observed He I line intensities into a He abundance. Neglecting or misestimating them may lead to systematic errors in the Y_p determination that can be larger than the statistical errors. Different empirical methods have been used to derive the He primordial abundance (e.g. Izotov et al. 1994, 1997; Izotov & Thuan 2010; Peimbert et al. 2007; Aver et al. 2010, 2011, 2012, 2013). All of them make use of analytical fits for various physical processes (e.g. Izotov et al. 2006), including fits of He I and H I emissivities and of effects that make the observed line intensities deviate from their recombination values. These effects include for instance collisional and fluorescent enhancements of He I recombination lines and underlying He I stellar absorption lines. A detailed discussion of the role of each of these various effects is given in Izotov et al. (2007). Most of the known systematic effects have generally been taken into account in the most recent work on the determination of the helium abundance (e.g. Izotov et al. 2007; Izotov & Thuan 2010; Peimbert et al. 2007; Aver et al. 2010, 2012, 2013).

Based on the HeBCD sample, Izotov & Thuan (2010) found $Y_p = 0.2565 \pm 0.003$ (1σ). Using a restricted subsample of 22 objects selected from the same HeBCD sample of Izotov et al. (2007), Aver et al. (2012) derived a value $Y_p = 0.2534 \pm 0.0083$. Subsequent to this work, a new set of He I line emissivities was put forward by Porter et al. (2013). With this new emissivity set, Izotov et al. (2013) derived $Y_p = 0.254 \pm 0.003$ (1σ) based on a large sample, while Aver et al. (2013) obtained $Y_p = 0.2465 \pm 0.0097$ with the same restricted sample. We note that, Izotov & Thuan (2010) and Izotov et al. (2013), by using much larger samples of H II regions as compared to Aver et al. (2012) and Aver et al. (2013), determined Y_p with considerably smaller statistical errors. Taking into account the statistical and systematic errors in the Y_p determination, one can conclude that these latest determinations of Y_p are broadly (at the 1σ level for the value by Aver et al. 2013) consistent with the prediction of SBBN based on the cosmic background (CMB) measurements of Planck, $Y_p = 0.2477 \pm 0.0001$ (Ade et al. 2013).

Izotov et al. (2013) have also checked the validity of the above overall procedure for determining the He abundance by using photoionisation CLOUDY models (Ferland et al. 1998, 2013). Since a photoionisation code such as CLOUDY takes into account all the processes affecting the He I line intensities, it should produce in principle model H II regions that are very similar in properties to real H II regions. Izotov et al. (2013) showed that the empirical method used by, e.g. Izotov & Thuan (2010), does reproduce very well the input CLOUDY helium mass fraction Y . However, the physical conditions, as characterized by the electron temperature $T_e(\text{He}^+)$ and the electron number density $N_e(\text{He}^+)$ are rather poorly reproduced, if only the 5 strongest $\lambda 3889$, $\lambda 4471$, $\lambda 5876$, $\lambda 6678$, and $\lambda 7065$ He I emission lines in the optical range are used for the χ^2 minimisation in the determination of best Y values. Izotov et al. (2013) suggested that adding the strong near-infrared He I $\lambda 10830$ emission line may greatly improve the determination of physical conditions and Y because of the very strong dependence of the intensity of this line on electron number density, and hence diminish the systematic uncertainties.

In this paper, we present for the first time near-infrared (NIR) observations of a large sample of high-excitation low-metallicity galaxies, aiming to improve the primordial He abundance determination by including the He I $\lambda 10830$ emission line, as suggested by Izotov et al. (2013). In sect. 2, we describe the observations and data reduction of our sample. In Sect. 3, we discuss the method for Y determination. In Sect. 4, we present the linear regressions $Y - \text{O/H}$ and derive the primordial He mass fraction Y_p . Cosmological implications of the derived Y_p are discussed in Sect. 5. In particular, we obtain the effective number of neutrino species N_{eff} and discuss constraints on the possible presence of "dark radiation". Section 6 summarises our results.

2 THE SAMPLE

Our sample consists of 45 H II regions in 43 low-metallicity emission-line galaxies. The general characteristics of the sample galaxies are shown in Table 1.

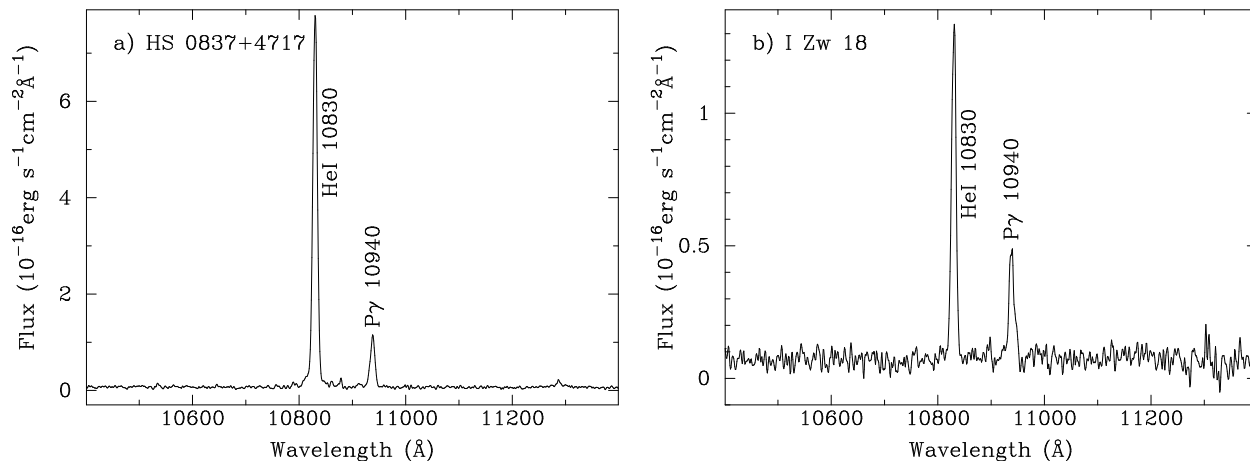


Figure 1. Representative APO spectra of H II regions showing the He I $\lambda 10830\text{\AA}$ and $P\gamma 10940\text{\AA}$ emission lines. The spectrum in (a) is that of a high-density H II region while the one in (b) is that of low-density H II region.

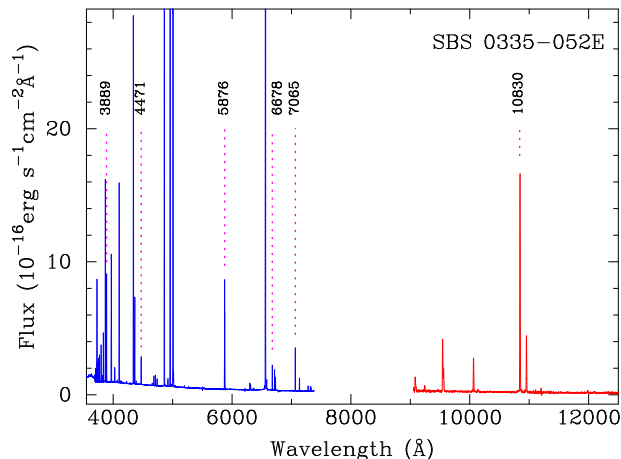


Figure 2. Redshift-corrected spectra of SBS 0335-052E in the optical range (blue) and in the near-infrared range (red) obtained with the 8.2m Very Large Telescope (VLT) and the 8.4m Large Binocular Telescope (LBT), respectively. The He I emission lines are marked by vertical dotted lines and labelled.

2.1 Observations and data reduction

2.1.1 Spectroscopic data

Our near-infrared spectroscopic data come from three sources.

The majority of the near-infrared spectra of our sample galaxies were obtained with the 3.5 m Apache Point Observatory (APO) telescope, in conjunction with the TripleSpec spectrograph, on a number of nights during the 2008 – 2013 period. TripleSpec (Wilson et al. 2004) is a cross-dispersed NIR spectrograph that provides simultaneous continuous wavelength coverage from 0.90 to $2.46\ \mu\text{m}$ in five spectral orders during a single exposure. A $1''.1 \times 43''$ slit was used, resulting in a resolving power of 3500. During the course of each night, several A0V standard stars were observed for flux calibration and correction for telluric absorption. Spectra of Ar comparison arcs were also obtained for wavelength calibration. Since all observed targets are smaller than the length of the slit, the nod-on-slit technique was used to acquire the sky spectrum. Objects were observed by nodding

between two positions A and B along the slit, following the ABBA sequence, and with an integration time of 200 s or 300 s at each position.

The APO telescope is not large enough to obtain good NIR spectra for the faintest galaxies, with SDSS $g \geq 17$ mag. These also tend to be the lowest-metallicity galaxies which play an important role in the determination of Y_p . We have thus observed eight low-metallicity H II regions with the 8.4 m Large Binocular Telescope (LBT), in conjunction with the Lucifer spectrograph, on several nights during the 2008 – 2013 period. A $1''$ LS 600 slit was used, giving a resolving power of 8460 in the J -band. Various A0V standard stars were observed during each night for flux calibration and correction for telluric absorption. Spectra of Ar comparison arcs were also obtained for wavelength calibration. All observed targets are smaller than the length of the slit, therefore the nod-on-slit technique was used to acquire the sky spectrum. Objects were observed by nodding between two positions A and B along the slit, following the ABBA sequence, and with an integration time of 240 s at each position.

Finally, we have retrieved from the European South Observatory (ESO) data archives VLT/ISAAC NIR spectra for two objects and NTT/SOFI NIR spectra for another two objects.

In addition, all galaxies listed in Table 1 possess good optical spectra either obtained by our group in the past for the determination of the primordial helium abundance, or from the SDSS spectral data base. The optical data is described in Izotov et al. (2007) and in other references given in Table 1. The complementary optical data are necessary to derive physical conditions and abundances in the sample galaxies.

2.1.2 Reduction procedures

We have carried out the reduction of the data according to the following procedures. The two-dimensional spectra were first cleaned for cosmic ray hits using the IRAF¹ routine

¹ IRAF is distributed by National Optical Astronomical Observatory, which is operated by the Association of Universities for

Table 1. General characteristics.

Name	R.A. (J2000)	Dec. (J2000)	Redshift	12+logO/H	References ^a	Other names
CGCG 007–025	09:44:01.9	−00:38:32	0.0048	7.79	1,2	SHOC 270
Haro 3	10:45:22.4	+55:57:37	0.0031	8.37	1,2	NGC 3353, Mrk 35, SBS 1042+562
HS 0837+4717	08:40:29.9	+47:07:10	0.0420	7.62	1,2	SHOC 220
HS 1734+5704	17:35:01.2	+57:03:09	0.0472	8.10	2	SHOC 579
I Zw 18 SE	09:34:02.0	+55:14:28	0.0026	7.23	2,3,4	UGCA 116, Mrk 116, SBS 0930+554
J0024+1404	00:24:26.0	+14:04:10	0.0142	8.40	2	HS0021+1347
J0115−0051	01:15:33.8	−00:51:31	0.0056	8.38	2	H II region in NGC 450
J0301−0052	03:01:49.0	−00:52:57	0.0073	7.59	2	
J0519+0007	05:19:02.6	+00:07:30	0.0444	7.43	1,5	
J1038+5330	10:38:44.9	+53:30:05	0.0032	8.37	2	H II region in NGC 3310
J1203−0342	12:03:51.1	−03:42:35	0.0130	8.49	2	
J1253−0313	12:53:06.0	−03:12:59	0.0228	8.04	2	SHOC 391
J1624−0022	16:24:10.1	−00:22:03	0.0313	8.20	2	SHOC 536
KUG 0952+418	09:55:45.6	+41:34:30	0.0157	8.40	2	HS 0952+4148
Mrk 36	11:04:58.3	+29:08:23	0.0022	7.81	2,6	UGCA 225, Haro 4, KUG 1102+294
Mrk 59	12:59:00.3	+34:50:42	0.0026	8.03	2,3	NGC 4861, Arp 209, I Zw 49
Mrk 71	07:28:42.8	+69:11:21	0.0004	7.89	3	NGC 2363
Mrk 162	11:05:08.1	+44:44:47	0.0215	8.12	2,6	KUG 1102+450, CG 1366
Mrk 209	12:26:15.9	+48:29:37	0.0009	7.81	2,3	UGCA 281, I Zw 36, Haro 29
Mrk 259	13:28:44.0	+43:55:51	0.0279	8.08	2	HS 1326+4411
Mrk 450	13:14:48.3	+34:52:51	0.0029	8.25	1,2	UGC 8323, VV 616, HS 1312+3508
Mrk 490	15:46:30.7	+45:59:54	0.0089	8.21	2	
Mrk 689	15:36:19.4	+30:40:56	0.0058	8.15	2	CG 1307
Mrk 930	23:31:58.3	+28:56:50	0.0183	8.09	6	
Mrk 1315	12:15:18.6	+20:38:27	0.0028	8.28	1,2	KUG 1212+209B
Mrk 1329	12:37:03.0	+06:55:36	0.0054	8.29	1,2	IC 3591, Tol 1234+072
Mrk 1448	11:34:45.7	+50:06:03	0.0260	8.27	2	SBS 1132+503
Mrk 1486	13:59:50.9	+57:26:23	0.0338	7.95	2	SBS 1358+576
NGC 1741	05:01:38.3	−04:15:25	0.0135	8.11	6	Mrk 1089, Arp 259, VV 524, VV 565
SBS 0335−052E	03:37:44.0	−05:02:40	0.0135	7.14–7.30	4,5,6,7	
SBS 0940+544	09:44:16.6	+54:11:34	0.0055	7.46	8,9	
SBS 1030+583	10:34:10.1	+58:03:49	0.0076	7.81	2,3	Mrk 1434, KUG 1030+583
SBS 1135+581	11:38:35.7	+57:52:27	0.0032	8.07	8	Mrk 1450, VII Zw 415
SBS 1152+579	11:55:28.3	+57:39:52	0.0179	7.90	2,8	Mrk 193, VII Zw 415
SBS 1222+614	12:25:05.4	+61:09:11	0.0024	7.98	2,3	
SBS 1415+437	14:17:01.4	+43:30:05	0.0020	7.60	8,10	
SBS 1428+457	14:30:12.2	+45:32:32	0.0078	8.41	2	CG 453
SBS 1437+370	14:39:05.4	+36:48:22	0.0019	7.94	3	Mrk 475
Tol 1214−277	12:17:17.1	−28:02:33	0.0260	7.55	5,11,12	Tol 21
Tol 65	12:25:46.9	−36:14:01	0.0094	7.55	5,11,12	Tol 1223-359
Tol 2138−405	21:41:21.8	−40:19:06	0.0581	8.03	5	
Tol 2146−391	21:49:48.2	−38:54:09	0.0294	7.83	5	
UM 311	01:15:34.4	−00:51:46	0.0056	7.83	2,6	SHOC 56

^aReferences of optical spectra.

References: (1) Izotov & Thuan (2004); (2) SDSS data base; (3) Izotov et al. (1997); (4) Izotov et al. (1999); (5) Guseva et al. (2011); (6) Izotov & Thuan (1998); (7) Izotov et al. (2009); (8) Izotov et al. (1994); (9) Izotov et al. (2007); (10) Guseva et al. (2003); (11) Izotov et al. (2001); (12) Izotov et al. (2004).

CRMEDIAN. Then all A and B frames were separately co-added and the resulting B frame was subtracted from the resulting A frame. Finally, the (negative) spectrum at position B was adjusted to the (positive) spectrum at position A and subtracted from it. The same reduction scheme was applied to the standard stars. We then use the IRAF routines IDENTIFY, REIDENTIFY, FITCOORD, and TRANSFORM to perform wavelength calibration and correction for distortion and tilt for each frame. For all galaxies, a one-dimensional

spectrum was extracted from the two-dimensional frames using the APALL IRAF routine.

Flux calibration and correction for telluric absorption were performed by first multiplying the one-dimensional spectrum of each galaxy by the synthetic absolute spectral distribution of the standard star, smoothed to the same spectral resolution, and then by dividing the result by the observed one-dimensional spectrum of the same star. Since there does not exist published absolute spectral energy distributions of the standard stars that were used, we have simply scaled the synthetic absolute SED of the star Vega (α Lyrae), also of A0V spectral type, to the brightness of the standard star.

Table 2. He I $\lambda 10830\text{\AA}$ and P γ $\lambda 10940\text{\AA}$ emission-line parameters.

Name	He I $\lambda 10830\text{\AA}$		P γ $\lambda 10940\text{\AA}$		$F(\text{He I})/F(\text{P}\gamma)$	Telescope/Instrument
	F^a	EW ^b	F^a	EW ^b		
CGCG 007–025	150.0 \pm 0.8	383 \pm 2	40.7 \pm 0.5	160 \pm 2	3.69 \pm 0.05	3.5m APO/Triplespec
Haro 3	786.0 \pm 1.7	221 \pm 1	320.8 \pm 1.3	90 \pm 1	2.45 \pm 0.02	3.5m APO/Triplespec
HS 0837+4717	162.1 \pm 0.6	1190 \pm 5	21.8 \pm 0.4	146 \pm 4	7.43 \pm 0.13	LBT/Lucifer
HS 1734+5704	170.9 \pm 2.6	708 \pm 2	47.8 \pm 0.8	146 \pm 2	3.58 \pm 0.08	3.5m APO/Triplespec
I Zw 18 SE	27.4 \pm 0.4	209 \pm 4	9.5 \pm 0.4	57 \pm 3	2.90 \pm 0.12	LBT/Lucifer
J0024+1404	54.1 \pm 0.9	40 \pm 1	20.6 \pm 0.8	17 \pm 1	2.63 \pm 0.11	3.5m APO/Triplespec
J0115–0051	295.1 \pm 1.3	600 \pm 2	116.2 \pm 0.9	243 \pm 1	2.54 \pm 0.02	3.5m APO/Triplespec
J0301–0052	10.2 \pm 0.2	150 \pm 3	5.1 \pm 0.2	54 \pm 2	2.01 \pm 0.08	LBT/Lucifer
J0519+0007	94.3 \pm 0.4	927 \pm 5	13.9 \pm 0.3	151 \pm 4	6.81 \pm 0.13	LBT/Lucifer
J1038+5330	389.6 \pm 4.0	27 \pm 1	151.8 \pm 3.7	12 \pm 1	2.57 \pm 0.07	3.5m APO/Triplespec
J1203–0342	62.9 \pm 1.0	42 \pm 1	25.4 \pm 0.8	17 \pm 1	2.48 \pm 0.09	3.5m APO/Triplespec
J1253–0313	1045.0 \pm 1.8	1050 \pm 2	173.1 \pm 1.7	149 \pm 1	6.04 \pm 0.07	3.5m APO/Triplespec
J1624–0022	47.6 \pm 0.8	98 \pm 2	18.1 \pm 0.6	50 \pm 2	2.64 \pm 0.10	3.5m APO/Triplespec
KUG 0952+418	46.8 \pm 0.8	56 \pm 1	15.6 \pm 0.6	18 \pm 1	3.00 \pm 0.13	3.5m APO/Triplespec
Mrk 36	89.1 \pm 0.9	95 \pm 1	37.5 \pm 0.6	42 \pm 1	2.38 \pm 0.05	3.5m APO/Triplespec
Mrk 59	601.7 \pm 1.5	284 \pm 1	243.8 \pm 1.0	125 \pm 1	2.47 \pm 0.02	3.5m APO/Triplespec
Mrk 71	2055.0 \pm 2.2	978 \pm 1	573.2 \pm 1.4	313 \pm 1	3.59 \pm 0.01	3.5m APO/Triplespec
Mrk 162	174.2 \pm 1.1	105 \pm 1	66.3 \pm 1.1	39 \pm 1	2.63 \pm 0.05	3.5m APO/Triplespec
Mrk 209	168.6 \pm 0.9	376 \pm 2	55.3 \pm 0.6	127 \pm 2	3.05 \pm 0.04	3.5m APO/Triplespec
Mrk 259	106.6 \pm 1.5	101 \pm 2	35.5 \pm 1.5	80 \pm 2	3.01 \pm 0.06	3.5m APO/Triplespec
Mrk 450	205.4 \pm 0.9	711 \pm 4	69.3 \pm 0.7	205 \pm 3	2.96 \pm 0.03	3.5m APO/Triplespec
Mrk 490	60.2 \pm 1.2	467 \pm 3	20.3 \pm 1.0	120 \pm 2	2.97 \pm 0.15	3.5m APO/Triplespec
Mrk 689	15.6 \pm 0.5	52 \pm 1	6.6 \pm 0.5	21 \pm 1	2.35 \pm 0.18	3.5m APO/Triplespec
Mrk 930	121.4 \pm 0.9	77 \pm 1	47.5 \pm 0.9	30 \pm 1	2.56 \pm 0.05	3.5m APO/Triplespec
Mrk 1315	169.6 \pm 0.9	441 \pm 2	74.5 \pm 0.7	179 \pm 4	2.28 \pm 0.03	3.5m APO/Triplespec
Mrk 1329	172.0 \pm 0.9	313 \pm 1	60.4 \pm 0.7	106 \pm 1	2.85 \pm 0.04	3.5m APO/Triplespec
Mrk 1448	80.6 \pm 1.0	106 \pm 2	27.5 \pm 1.6	36 \pm 2	2.94 \pm 0.18	3.5m APO/Triplespec
Mrk 1486	85.5 \pm 1.3	71 \pm 1	30.1 \pm 0.6	26 \pm 1	2.84 \pm 0.07	3.5m APO/Triplespec
NGC 1741 #1	234.4 \pm 1.4	138 \pm 1	87.5 \pm 1.1	55 \pm 1	2.68 \pm 0.04	3.5m APO/Triplespec
NGC 1741 #2	302.0 \pm 1.6	175 \pm 1	108.0 \pm 1.2	62 \pm 1	2.80 \pm 0.04	3.5m APO/Triplespec
SBS 0335–052E #1+2	382.7 \pm 0.6	618 \pm 1	95.5 \pm 0.4	163 \pm 1	4.01 \pm 0.02	LBT/Lucifer
SBS 0335–052E #7	25.8 \pm 0.4	432 \pm 8	6.7 \pm 0.3	169 \pm 9	3.86 \pm 0.18	LBT/Lucifer
SBS 0940+544	37.7 \pm 0.4	383 \pm 3	12.2 \pm 0.3	139 \pm 4	3.09 \pm 0.09	LBT/Lucifer
SBS 1030+583	53.2 \pm 0.4	101 \pm 1	20.8 \pm 0.4	41 \pm 1	2.55 \pm 0.05	LBT/Lucifer
SBS 1135+581	180.3 \pm 1.0	106 \pm 1	82.7 \pm 0.7	60 \pm 1	2.18 \pm 0.02	3.5m APO/Triplespec
SBS 1152+579	169.9 \pm 0.6	742 \pm 3	30.6 \pm 0.5	137 \pm 3	5.55 \pm 0.09	3.5m APO/Triplespec
SBS 1222+614	134.2 \pm 0.9	95 \pm 1	53.1 \pm 0.7	43 \pm 1	2.53 \pm 0.04	3.5m APO/Triplespec
SBS 1415+437	94.9 \pm 0.6	297 \pm 2	30.9 \pm 0.5	95 \pm 2	3.07 \pm 0.05	3.5m APO/Triplespec
SBS 1428+457	154.0 \pm 0.9	95 \pm 1	60.6 \pm 0.7	37 \pm 1	2.54 \pm 0.04	3.5m APO/Triplespec
SBS 1437+370	84.6 \pm 1.0	137 \pm 3	29.4 \pm 0.8	40 \pm 2	2.88 \pm 0.08	3.5m APO/Triplespec
Tol 1214–277	14.4 \pm 0.1	414 \pm 3	4.6 \pm 0.1	145 \pm 3	3.12 \pm 0.08	VLT/ISAAC
Tol 65	58.2 \pm 0.4	778 \pm 3	12.4 \pm 0.2	188 \pm 2	4.70 \pm 0.07	VLT/ISAAC
Tol 2138–405	346.7 \pm 5.1	1042 \pm 9	59.0 \pm 2.8	157 \pm 9	5.88 \pm 0.29	NTT/SOFI
Tol 2146–391	60.5 \pm 0.5	449 \pm 3	17.1 \pm 0.6	134 \pm 2	3.54 \pm 0.13	NTT/SOFI
UM 311	44.0 \pm 0.6	223 \pm 4	20.2 \pm 0.5	94 \pm 3	2.18 \pm 0.05	3.5m APO/Triplespec

^a Observed flux in units $10^{-16} \text{ erg s}^{-1} \text{ cm}^{-2}$.^b Equivalent width in \AA .

The emission-line fluxes were measured using Gaussian fitting with the IRAF SPLOT routine. The line flux errors were estimated by Monte Carlo simulations in SPLOT, setting the number of trials to 200.

Two representative spectra, one of a high-density H II region (left) and the other of a low-density one (right) are shown in Fig. 1. The fluxes and equivalent widths of the He I $\lambda 10830\text{\AA}$ emission line, needed for the Y_p determination, and of the P γ $\lambda 10940\text{\AA}$ emission line, needed to adjust NIR and optical spectra, are presented in Table 2.

2.2 Physical conditions and heavy element abundances

We derived element abundances from the narrow emission-line fluxes, using the so-called direct method. This method is based on the determination of the electron temperature within the O^{2+} zone from the $[\text{O III}] \lambda 4363/(\lambda 4959 + \lambda 5007)$ line ratio. The fluxes in all optical spectra were corrected for both extinction, using the reddening curve of Cardelli et al. (1989), and underlying hydrogen stellar absorption, derived simultaneously by an iterative procedure described by Izotov et al. (1994) and using the observed

Table 3. Derived parameters for the He abundance determination.^a

Name	O/H $\times 10^5$	Y	$t_e(\text{O III})^b$	$t_e(\text{He}^+)^b$	$N_e(\text{S II})^c$	$N_e(\text{He}^+)^c$	$\tau(\lambda 3889)$	$ICF(\text{He})^d$
CGCG 007–025 ^e	5.8 \pm 0.2	0.2568 \pm 0.0031	1.64 \pm 0.02	1.69 \pm 0.01	124 \pm 38	125 \pm 2	1.29 \pm 0.03	0.9940
CGCG 007–025 ^e	5.7 \pm 0.1	0.2587 \pm 0.0040	1.70 \pm 0.02	1.60 \pm 0.04	153 \pm 57	130 \pm 6	1.92 \pm 0.01	0.9938
Haro 3	19.0 \pm 0.7	0.2637 \pm 0.0030	1.02 \pm 0.01	1.08 \pm 0.02	175 \pm 32	35 \pm 3	2.14 \pm 0.10	1.0080
HS 0837+4717 ^e	4.8 \pm 0.1	0.2455 \pm 0.0035	1.93 \pm 0.02	1.81 \pm 0.05	343 \pm 93	541 \pm 24	4.66 \pm 0.01	0.9941
HS 0837+4717 ^e	5.1 \pm 0.1	0.2577 \pm 0.0046	1.86 \pm 0.02	1.75 \pm 0.01	513 \pm 140	520 \pm 1	5.00 \pm 0.01	0.9956
HS 0837+4717 ^e	4.6 \pm 0.1	0.2602 \pm 0.0047	1.91 \pm 0.03	1.81 \pm 0.05	287 \pm 106	484 \pm 22	5.00 \pm 0.03	0.9949
HS 1734+5704	14.8 \pm 0.3	0.2609 \pm 0.0035	1.25 \pm 0.01	1.19 \pm 0.01	262 \pm 50	208 \pm 6	5.00 \pm 0.04	0.9972
I Zw 18 SE ^e	1.6 \pm 0.1	0.2515 \pm 0.0068	1.86 \pm 0.06	1.91 \pm 0.04	10 \pm 10	47 \pm 2	0.03 \pm 0.19	0.9984
I Zw 18 SE ^e	1.7 \pm 0.2	0.2596 \pm 0.0084	1.75 \pm 0.08	1.81 \pm 0.03	11 \pm 68	43 \pm 1	0.82 \pm 0.04	1.0004
I Zw 18 SE ^e	1.8 \pm 0.1	0.2446 \pm 0.0050	1.70 \pm 0.03	1.76 \pm 0.02	55 \pm 70	60 \pm 4	0.14 \pm 0.14	0.9966
J0024+1404	19.7 \pm 3.6	0.2705 \pm 0.0127	0.98 \pm 0.05	1.05 \pm 0.02	40 \pm 58	56 \pm 10	0.03 \pm 0.10	1.0123
J0115–0051	19.2 \pm 1.5	0.2605 \pm 0.0060	1.00 \pm 0.02	1.07 \pm 0.01	141 \pm 52	58 \pm 3	1.48 \pm 0.05	1.0035
J0301–0052	5.2 \pm 0.7	0.2542 \pm 0.0256	1.60 \pm 0.10	1.51 \pm 0.01	69 \pm 283	11 \pm 1	1.37 \pm 0.37	0.9962
J0519+0007 ^e	3.2 \pm 0.1	0.2396 \pm 0.0047	2.03 \pm 0.03	1.90 \pm 0.09	335 \pm 208	460 \pm 32	3.40 \pm 0.18	0.9943
J0519+0007 ^e	3.3 \pm 0.1	0.2521 \pm 0.0027	1.99 \pm 0.02	1.88 \pm 0.01	475 \pm 60	467 \pm 1	5.01 \pm 0.01	0.9955
J1038+5330	16.4 \pm 1.4	0.2473 \pm 0.0046	1.00 \pm 0.03	1.06 \pm 0.01	200 \pm 40	116 \pm 5	0.45 \pm 0.01	1.0194
J1203–0342	26.1 \pm 14.8	0.2718 \pm 0.0165	0.89 \pm 0.16	0.95 \pm 0.04	76 \pm 70	48 \pm 16	0.09 \pm 0.55	1.0177
J1253–0313	9.4 \pm 0.2	0.2512 \pm 0.0028	1.38 \pm 0.01	1.43 \pm 0.06	495 \pm 58	510 \pm 52	4.94 \pm 0.10	0.9965
J1624–0022	14.3 \pm 0.4	0.2577 \pm 0.0044	1.17 \pm 0.01	1.21 \pm 0.02	58 \pm 38	63 \pm 6	1.54 \pm 0.02	1.0027
KUG 0952+418	28.0 \pm 5.2	0.2678 \pm 0.0161	1.00 \pm 0.08	0.97 \pm 0.04	73 \pm 70	172 \pm 24	1.78 \pm 0.03	1.0189
Mrk 36 ^e	8.1 \pm 0.4	0.2501 \pm 0.0092	1.51 \pm 0.04	1.42 \pm 0.02	28 \pm 49	26 \pm 1	3.04 \pm 0.01	1.0000
Mrk 36 ^e	5.6 \pm 0.2	0.2493 \pm 0.0076	1.54 \pm 0.03	1.60 \pm 0.03	46 \pm 56	16 \pm 3	0.25 \pm 0.09	0.9966
Mrk 59 ^e	9.2 \pm 0.2	0.2555 \pm 0.0028	1.35 \pm 0.01	1.41 \pm 0.01	84 \pm 32	29 \pm 1	1.05 \pm 0.07	0.9969
Mrk 59 ^e	10.0 \pm 0.3	0.2465 \pm 0.0047	1.31 \pm 0.01	1.37 \pm 0.01	83 \pm 62	42 \pm 3	0.52 \pm 0.06	0.9975
Mrk 71	6.8 \pm 0.2	0.2542 \pm 0.0026	1.57 \pm 0.01	1.62 \pm 0.02	122 \pm 36	126 \pm 5	1.32 \pm 0.01	0.9956
Mrk 162	11.8 \pm 0.9	0.2586 \pm 0.0079	1.17 \pm 0.03	1.23 \pm 0.03	80 \pm 54	61 \pm 5	0.07 \pm 0.09	1.0031
Mrk 209 ^e	6.7 \pm 0.1	0.2475 \pm 0.0027	1.63 \pm 0.02	1.56 \pm 0.01	75 \pm 34	91 \pm 4	0.01 \pm 0.08	0.9952
Mrk 209 ^e	5.8 \pm 0.2	0.2643 \pm 0.0050	1.64 \pm 0.02	1.70 \pm 0.01	68 \pm 70	50 \pm 5	0.03 \pm 0.05	0.9965
Mrk 259	13.9 \pm 0.9	0.2578 \pm 0.0089	1.21 \pm 0.04	1.16 \pm 0.05	152 \pm 66	132 \pm 12	0.10 \pm 0.29	1.0035
Mrk 450 ^e	15.8 \pm 0.4	0.2523 \pm 0.0034	1.17 \pm 0.01	1.15 \pm 0.01	128 \pm 34	135 \pm 4	2.97 \pm 0.03	0.9985
Mrk 450 ^e	15.2 \pm 0.6	0.2643 \pm 0.0065	1.16 \pm 0.02	1.22 \pm 0.01	171 \pm 86	94 \pm 2	2.34 \pm 0.01	1.0000
Mrk 490	18.7 \pm 5.0	0.2615 \pm 0.0206	1.06 \pm 0.14	1.02 \pm 0.05	32 \pm 56	159 \pm 22	0.48 \pm 1.01	1.0125
Mrk 689	12.3 \pm 1.0	0.2530 \pm 0.0106	1.20 \pm 0.03	1.26 \pm 0.02	115 \pm 76	32 \pm 1	0.13 \pm 0.22	1.0033
Mrk 930	11.8 \pm 0.9	0.2590 \pm 0.0082	1.23 \pm 0.04	1.25 \pm 0.01	59 \pm 46	42 \pm 4	0.01 \pm 0.07	1.0038
Mrk 1315 ^e	16.4 \pm 0.4	0.2594 \pm 0.0029	1.10 \pm 0.01	1.15 \pm 0.01	17 \pm 18	10 \pm 3	0.63 \pm 0.06	0.9977
Mrk 1315 ^e	18.1 \pm 0.8	0.2615 \pm 0.0051	1.06 \pm 0.01	1.12 \pm 0.01	86 \pm 60	11 \pm 2	0.55 \pm 0.05	0.9980
Mrk 1329 ^e	18.0 \pm 0.5	0.2613 \pm 0.0029	1.07 \pm 0.01	1.10 \pm 0.01	20 \pm 19	106 \pm 4	1.17 \pm 0.04	0.9994
Mrk 1329 ^e	19.0 \pm 0.9	0.2560 \pm 0.0056	1.04 \pm 0.02	1.11 \pm 0.01	87 \pm 59	118 \pm 3	0.72 \pm 0.10	0.9998
Mrk 1448	15.6 \pm 1.3	0.2599 \pm 0.0089	1.08 \pm 0.03	1.14 \pm 0.02	61 \pm 59	125 \pm 6	0.07 \pm 0.16	1.0069
Mrk 1486	8.4 \pm 0.5	0.2631 \pm 0.0119	1.40 \pm 0.04	1.44 \pm 0.05	18 \pm 50	58 \pm 9	0.76 \pm 0.05	0.9997
NGC 1741 #1	11.0 \pm 1.7	0.2680 \pm 0.0088	1.11 \pm 0.07	1.16 \pm 0.01	88 \pm 46	72 \pm 4	0.03 \pm 0.03	1.0093
SBS 0335–052E #1+2 ^e	2.4 \pm 0.1	0.2562 \pm 0.0054	2.00 \pm 0.04	1.88 \pm 0.05	313 \pm 180	103 \pm 5	4.70 \pm 0.06	0.9948
SBS 0335–052E #1+2 ^e	2.1 \pm 0.1	0.2611 \pm 0.0030	2.00 \pm 0.02	2.06 \pm 0.05	321 \pm 69	85 \pm 3	4.74 \pm 0.02	0.9958
SBS 0335–052E #1+2 ^e	2.3 \pm 0.1	0.2603 \pm 0.0031	2.06 \pm 0.03	1.96 \pm 0.02	296 \pm 82	92 \pm 1	3.28 \pm 0.04	0.9956
SBS 0335–052E #1+2 ^e	2.1 \pm 0.1	0.2543 \pm 0.0035	2.08 \pm 0.03	2.13 \pm 0.01	237 \pm 104	90 \pm 1	4.99 \pm 0.02	0.9967
SBS 0335–052E #1+2 ^e	2.0 \pm 0.1	0.2559 \pm 0.0026	2.03 \pm 0.02	2.08 \pm 0.03	10 \pm 10	87 \pm 5	5.00 \pm 0.01	0.9941
SBS 0335–052E #1+2 ^e	2.1 \pm 0.1	0.2584 \pm 0.0026	2.10 \pm 0.03	1.98 \pm 0.04	170 \pm 47	119 \pm 4	4.99 \pm 0.01	0.9940
SBS 0335–052E #1+2 ^e	2.4 \pm 0.1	0.2604 \pm 0.0032	2.03 \pm 0.03	1.90 \pm 0.03	421 \pm 88	117 \pm 1	4.98 \pm 0.01	0.9954
SBS 0335–052E #1+2 ^e	2.4 \pm 0.1	0.2545 \pm 0.0033	2.03 \pm 0.03	1.90 \pm 0.03	215 \pm 65	140 \pm 3	1.45 \pm 0.06	1.0003
SBS 0335–052E #7 ^e	1.7 \pm 0.1	0.2527 \pm 0.0048	1.97 \pm 0.04	1.85 \pm 0.04	99 \pm 116	122 \pm 2	0.02 \pm 0.03	0.9927
SBS 0335–052E #7 ^e	1.6 \pm 0.2	0.2457 \pm 0.0097	2.00 \pm 0.10	1.87 \pm 0.08	352 \pm 442	135 \pm 10	0.03 \pm 0.09	0.9935
SBS 0940+544 ^e	3.0 \pm 0.1	0.2601 \pm 0.0065	1.99 \pm 0.04	1.95 \pm 0.01	167 \pm 118	45 \pm 1	0.40 \pm 0.07	0.9938
SBS 0940+544 ^e	3.3 \pm 0.1	0.2556 \pm 0.0037	1.86 \pm 0.02	1.87 \pm 0.04	166 \pm 58	56 \pm 3	0.02 \pm 0.09	0.9947
SBS 1030+583 ^e	7.5 \pm 0.2	0.2536 \pm 0.0052	1.56 \pm 0.02	1.47 \pm 0.02	10 \pm 10	43 \pm 5	0.45 \pm 0.08	0.9997
SBS 1030+583 ^e	6.4 \pm 0.4	0.2533 \pm 0.0119	1.52 \pm 0.04	1.57 \pm 0.04	80 \pm 123	35 \pm 3	0.03 \pm 0.33	0.9991
SBS 1135+581	12.8 \pm 0.3	0.2579 \pm 0.0034	1.26 \pm 0.01	1.22 \pm 0.01	49 \pm 32	10 \pm 2	1.00 \pm 0.02	0.9996
SBS 1152+573 ^e	9.1 \pm 0.2	0.2399 \pm 0.0029	1.54 \pm 0.02	1.45 \pm 0.01	152 \pm 42	481 \pm 6	1.59 \pm 0.04	0.9963
SBS 1152+573 ^e	8.3 \pm 0.4	0.2506 \pm 0.0076	1.47 \pm 0.02	1.53 \pm 0.04	145 \pm 107	395 \pm 17	2.15 \pm 0.03	0.9968
SBS 1222+614	10.9 \pm 0.3	0.2495 \pm 0.0053	1.40 \pm 0.02	1.33 \pm 0.03	74 \pm 50	52 \pm 3	0.51 \pm 0.01	0.9985
SBS 1415+437 ^e	4.0 \pm 0.1	0.2522 \pm 0.0037	1.64 \pm 0.02	1.69 \pm 0.02	56 \pm 39	79 \pm 2	0.83 \pm 0.05	0.9956
SBS 1415+437 ^e	4.7 \pm 0.1	0.2510 \pm 0.0034	1.70 \pm 0.02	1.60 \pm 0.01	108 \pm 42	89 \pm 2	1.09 \pm 0.03	0.9955
SBS 1415+437 ^e	4.7 \pm 0.1	0.2511 \pm 0.0040	1.68 \pm 0.02	1.58 \pm 0.02	83 \pm 42	91 \pm 4	0.97 \pm 0.01	0.9949
SBS 1428+457	21.9 \pm 2.3	0.2659 \pm 0.0095	0.99 \pm 0.04	1.04 \pm 0.03	94 \pm 66	59 \pm 7	0.48 \pm 0.16	1.0130

Table 3. Continued.

Name	O/H $\times 10^5$	Y	$t_e(\text{O III})^b$	$t_e(\text{He}^+)^b$	$N_e(\text{S II})^c$	$N_e(\text{He}^+)^c$	$\tau(\lambda 3889)$	$ICF(\text{He})^d$
SBS 1437+370	10.1 \pm 0.2	0.2574 \pm 0.0059	1.41 \pm 0.02	1.34 \pm 0.03	76 \pm 36	78 \pm 6	0.72 \pm 0.07	0.9970
Tol 1214–277 ^e	3.5 \pm 0.1	0.2563 \pm 0.0032	1.96 \pm 0.02	2.02 \pm 0.02	258 \pm 74	59 \pm 5	0.02 \pm 0.07	0.9942
Tol 1214–277 ^e	3.6 \pm 0.1	0.2518 \pm 0.0028	1.95 \pm 0.02	2.01 \pm 0.03	188 \pm 63	69 \pm 2	0.77 \pm 0.04	0.9937
Tol 1214–277 ^e	3.4 \pm 0.1	0.2527 \pm 0.0025	1.98 \pm 0.02	2.05 \pm 0.01	10 \pm 10	62 \pm 4	0.50 \pm 0.07	0.9934
Tol 65 ^e	3.4 \pm 0.1	0.2443 \pm 0.0033	1.72 \pm 0.02	1.78 \pm 0.03	21 \pm 26	242 \pm 6	0.17 \pm 0.05	0.9949
Tol 65 ^e	3.5 \pm 0.1	0.2440 \pm 0.0027	1.70 \pm 0.02	1.76 \pm 0.01	171 \pm 41	242 \pm 5	1.21 \pm 0.06	0.9934
Tol 2138–405 ^e	10.6 \pm 0.2	0.2548 \pm 0.0031	1.39 \pm 0.01	1.39 \pm 0.01	339 \pm 47	401 \pm 10	1.87 \pm 0.02	0.9960
Tol 2138–405 ^e	11.9 \pm 0.4	0.2591 \pm 0.0046	1.31 \pm 0.02	1.37 \pm 0.05	347 \pm 56	399 \pm 40	2.53 \pm 0.04	0.9973
Tol 2146–391 ^e	6.2 \pm 0.2	0.2553 \pm 0.0029	1.57 \pm 0.02	1.63 \pm 0.01	165 \pm 40	127 \pm 2	1.20 \pm 0.11	0.9949
Tol 2146–391 ^e	6.3 \pm 0.2	0.2481 \pm 0.0045	1.59 \pm 0.02	1.65 \pm 0.04	183 \pm 54	135 \pm 10	1.53 \pm 0.10	0.9946
UM 311 ^e	23.3 \pm 2.4	0.2579 \pm 0.0065	0.97 \pm 0.04	0.98 \pm 0.01	72 \pm 47	10 \pm 6	2.62 \pm 0.04	1.0020
UM 311 ^e	27.8 \pm 2.7	0.2618 \pm 0.0060	0.94 \pm 0.04	0.91 \pm 0.01	10 \pm 10	13 \pm 1	0.06 \pm 0.08	1.0181

^a Parameters are calculated for the case where all six He I emission lines $\lambda 3889$, $\lambda 4471$, $\lambda 5876$, $\lambda 6678$, $\lambda 7065$, and $\lambda 10830$ have been used for the χ^2 minimisation, and only the four He I emission lines $\lambda 4471$, $\lambda 5876$, $\lambda 6678$, and $\lambda 10830$ have been used for the determination of Y.

^b $t_e = 10^{-4}T_e$.

^c in cm^{-3} .

^d Uncertainties of $ICF(\text{He})$ are ~ 0.0025 (Izotov et al. 2013).

^e Multiple entries for the same galaxy refer to independent sets of spectroscopic data for that galaxy.

decrements of the narrow hydrogen Balmer lines. The extinction coefficient $C(\text{H}\beta)$ and equivalent width of hydrogen absorption lines $\text{EW}(\text{abs})$ are derived in such a way to obtain the closest agreement between the extinction-corrected and theoretical recombination hydrogen emission-line fluxes normalised to the $\text{H}\beta$ flux. It is assumed that $\text{EW}(\text{abs})$ is the same for all hydrogen lines. This assumption is justified by the evolutionary stellar population synthesis models of González Delgado et al. (2005).

The physical conditions, and the ionic and total heavy element abundances in the H II regions were derived following Izotov et al. (2006). In particular, for O^{2+} , Ne^{2+} , and Ar^{3+} abundances, we adopt the temperature $T_e(\text{O III})$ directly derived from the $[\text{O III}] \lambda 4363/(\lambda 4959 + \lambda 5007)$ emission-line ratio. The electron temperatures $T_e(\text{O II})$ and $T_e(\text{S III})$ were derived from the empirical relations by Izotov et al. (2006). $T_e(\text{O II})$ was used for the calculation of O^+ , N^+ , S^+ , and Fe^{2+} abundances and $T_e(\text{S III})$ for the calculation of S^{2+} , Cl^{2+} , and Ar^{2+} abundances. The electron number densities $N_e(\text{S II})$ were obtained from the $[\text{S II}] \lambda 6717/\lambda 6731$ emission-line ratios. The low-density limit holds for the H II regions that exhibit the emission lines considered here. The element abundances then do not depend sensitively on N_e . We use the ionisation correction factors ($ICFs$) from Izotov et al. (2006) to correct for unseen stages of ionisation and to derive the total O, N, Ne, S, Cl, Ar, and Fe abundances.

The physical conditions and heavy-element abundances for the most of the objects in our sample were derived in several previous studies by our group. The references to these studies are shown in Table 1. We have listed the main physical parameters along with their uncertainties in Table 3. These uncertainties were derived from the uncertainties of the optical line intensities given in our previous papers (references in Table 1), and from the uncertainties of the NIR line intensities given in Table 2. They were propagated to derive the oxygen and helium abundances.

Whenever there exists several observations of the same object in the optical range, we treat those as independent

observations to increase the statistics. The optical data obtained by our group have been supplemented by spectra from the Sloan Digital Sky Survey (SDSS). In total, our sample consists of 75 optical spectra which were combined with the 45 near-infrared spectra.

2.3 Adjustment of NIR to optical spectra

As the NIR and optical spectra were obtained with different telescopes and apertures at different times, we need to match them. The scale factor f needed to adjust the intensity of the He I $\lambda 10830\text{\AA}$ NIR line to the $\text{H}\beta$ intensity is defined by the following equation:

$$\frac{I(\text{He I } \lambda 10830)}{I(\text{H}\beta)} = f \times \frac{F(\text{He I } \lambda 10830)}{F(\text{P}\gamma \lambda 10940)} \quad (1)$$

In this equation, f is the theoretical value of the recombination line ratio $\text{P}\gamma/\text{H}\beta$ (Hummer & Storey 1992) which depends mainly on the electron temperature, but little on the electron density. Thus in the $N_e = 10^2\text{--}10^4 \text{ cm}^{-3}$ range, $f=9.04$ for $T_e = 10^4\text{K}$, and $f=8.11$ for $T_e = 2\times 10^4\text{K}$. $I(\text{He I } \lambda 10830)/I(\text{H}\beta)$ is the extinction-corrected ratio, and $F(\text{He I } \lambda 10830)/F(\text{P}\gamma \lambda 10940)$ is the observed ratio derived from Table 2. The He I $\lambda 10830$ and the $\text{P}\gamma \lambda 10940$ emission lines are very close in wavelength, so that differential extinction between these two lines is negligible. Uncertainties of the $F(\text{He I } \lambda 10830)/F(\text{P}\gamma \lambda 10940)$ ratios were propagated in the derivation of the He abundance.

Fig. 2 shows an example of the matching of the optical and NIR spectra for one galaxy, the BCD SBS 0335–052E. The He I lines used for the determination of the primordial helium abundance are indicated. The Figure shows that the intensity of the NIR line is considerably higher than those of the optical lines.

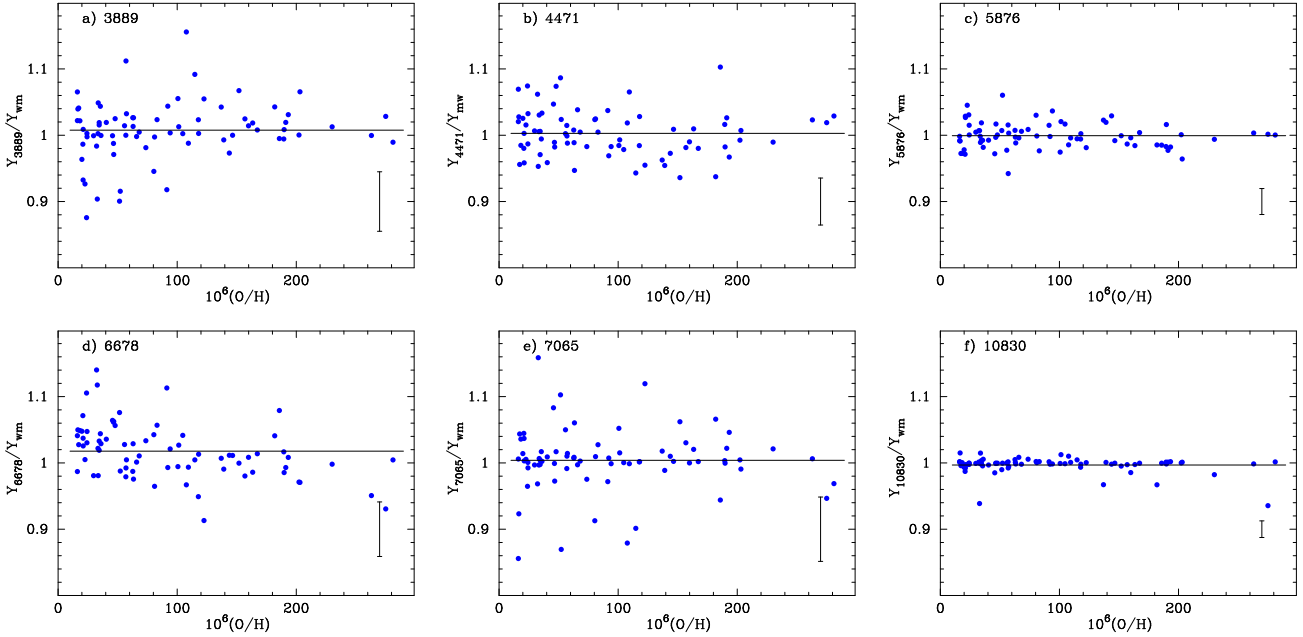


Figure 3. Ratios of $Y(\lambda)$ derived from individual He I emission lines to the weighted mean helium abundance Y_{wm} . All six He I emission lines were used for the χ^2 minimisation and Y_{wm} determination. Horizontal lines show a ratio of 1, and error bars are 1σ dispersions.

3 DETERMINING THE HE ABUNDANCE

3.1 Corrections for dust extinction, fluorescent and collisional excitation, ionisation structure and underlying stellar absorption

To carry out our empirical method to determine helium abundances in real H II regions, several effects need to be considered and corrections applied.

First, the Balmer decrement correction was used to simultaneously determine the dust extinction and equivalent widths of underlying stellar hydrogen absorption lines, as described e.g. in Izotov et al. (1994), and to correct line intensities for both effects. Second, since the spectra of extragalactic H II regions include both ionised gas and stellar emission, the underlying stellar He I absorption lines should be taken into account (see e.g. Izotov et al. 2007). Third, the He I emission lines should be corrected for fluorescent excitation, parametrised by the optical depth $\tau(\lambda 3889)$ of the He I $\lambda 3889$ emission line. We used the correction factors for fluorescent excitation derived by Benjamin et al. (1999, 2002).

To take into account the new set of He I emissivities of Porter et al. (2013), the collisional excitation of He I emission lines, the non-recombination contribution to hydrogen emission-line intensities, and the correction for the ionisation structure of the H II region, we have adopted the fits provided by Izotov et al. (2013).

The equivalent width of the He I $\lambda 4471$ absorption line is chosen to be $\text{EW}_{\text{abs}}(\lambda 4471) = 0.4\text{\AA}$, following González Delgado et al. (2005), Izotov & Thuan (2010), and Izotov et al. (2013). The equivalent widths of the other absorption lines in the optical range were fixed according to the ratios

$$\begin{aligned} \text{EW}_{\text{abs}}(\lambda 3889)/\text{EW}_{\text{abs}}(\lambda 4471) &= 1.0, \\ \text{EW}_{\text{abs}}(\lambda 5876)/\text{EW}_{\text{abs}}(\lambda 4471) &= 0.8, \end{aligned}$$

$$\begin{aligned} \text{EW}_{\text{abs}}(\lambda 6678)/\text{EW}_{\text{abs}}(\lambda 4471) &= 0.4, \\ \text{EW}_{\text{abs}}(\lambda 7065)/\text{EW}_{\text{abs}}(\lambda 4471) &= 0.4, \\ \text{EW}_{\text{abs}}(\lambda 10830)/\text{EW}_{\text{abs}}(\lambda 4471) &= 0.8. \end{aligned} \quad (2)$$

The $\text{EW}_{\text{abs}}(\lambda 5876) / \text{EW}_{\text{abs}}(\lambda 4471)$ and $\text{EW}_{\text{abs}}(\lambda 6678) / \text{EW}_{\text{abs}}(\lambda 4471)$ ratios were set equal to the values predicted for these ratios by a Starburst99 (Leitherer et al. 1999) instantaneous burst model with an age of 3 – 4 Myr and a heavy-element mass fraction $Z = 0.001 - 0.008$. We note that the value chosen for the $\text{EW}_{\text{abs}}(\lambda 5876) / \text{EW}_{\text{abs}}(\lambda 4471)$ ratio is consistent with the one given by González Delgado et al. (2005). Since the output high-resolution spectra in Starburst99 are calculated only for wavelengths $< 7000\text{\AA}$, we do not have a prediction for the $\text{EW}_{\text{abs}}(\lambda 7065) / \text{EW}_{\text{abs}}(\lambda 4471)$ ratio. We set it to be equal to 0.4, the value of the $\text{EW}_{\text{abs}}(\lambda 6678) / \text{EW}_{\text{abs}}(\lambda 4471)$ ratio. As for He I $\lambda 3889$, this line is blended with the hydrogen H8 $\lambda 3889$ line. Therefore, $\text{EW}_{\text{abs}}(\text{He I } \lambda 3889)$ cannot be estimated from the Starburst99 models. We assumed the value shown in Eq. 2.

No data are available for the EW_{abs} of the He I $\lambda 10830$ NIR line. Therefore, we have set it to be equal to the EW_{abs} of another strong line, the He I $\lambda 5876$ optical emission line. This assumption does not introduce an appreciable uncertainty in the He I $\lambda 10830$ emission-line flux, because the equivalent width of this line is generally high (Table 2).

3.2 Starburst ages and ionisation correction factors

The age t_{burst} of the starburst in the H II region needs to be derived. This is because the ionisation correction factors $ICF(\text{He})$ and the non-recombination contribution to hydrogen lines both depend on the starburst age (Izotov et al. 2013). As a first approximation, Izotov et al. (2013) used the relation between t_{burst} and $\text{EW}(\text{H}\beta)$ from the Starburst99 instantaneous burst models with a heavy-element mass frac-

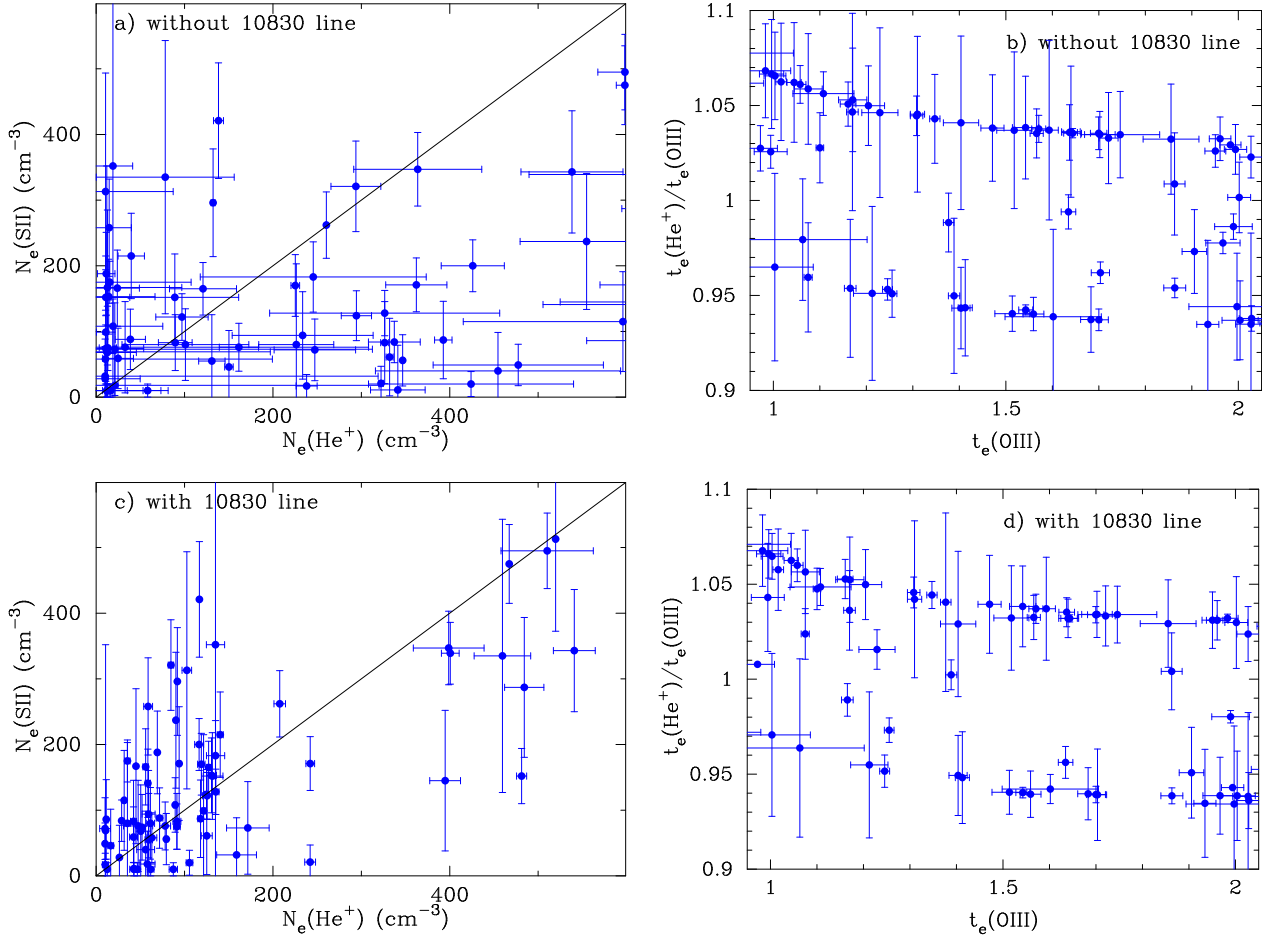


Figure 4. (a) Electron densities $N_e(\text{He}^+)$ derived from the χ^2 minimisation procedure versus $N_e(\text{S II})$ derived from the $[\text{S II}]$ line ratio. Only the five He I $\lambda 3889$, $\lambda 4471$, $\lambda 5876$, $\lambda 6678$, and $\lambda 7065$ optical emission lines have been used for the χ^2 minimisation. The NIR He I $\lambda 10830$ emission line has been excluded. $N_e(\text{He}^+)$ has been varied in the range 10 – 600 cm $^{-3}$. (b) Electron temperature ratios $T_e(\text{He}^+)/T_e(\text{O III})$ derived from the χ^2 minimisation procedure versus $T_e(\text{O III})$ derived from the O III line ratio. Here, $t_e = 10^{-4}T_e$. Only the five He I $\lambda 3889$, $\lambda 4471$, $\lambda 5876$, $\lambda 6678$, and $\lambda 7065$ optical emission lines have been used for the χ^2 minimisation. The NIR He I $\lambda 10830$ emission line has been excluded. $T_e(\text{He}^+)$ has been varied in the range 0.95 – 1.05 of the $\tilde{T}_e(\text{He}^+)$, where $\tilde{T}_e(\text{He}^+)$ is defined by Eq. 9. (c) and (d) Same as (a) and (b), respectively, except that the NIR He I $\lambda 10830$ emission line is now included, so that all six He I $\lambda 3889$, $\lambda 4471$, $\lambda 5876$, $\lambda 6678$, $\lambda 7065$, and $\lambda 10830$ emission lines are used for the χ^2 minimisation. 1σ errors bars are shown in all panels.

tion $Z = 0.004$ (Leitherer et al. 1999). They fitted this relation by the expression

$$t_{\text{burst}} = 167.6w^3 - 2296w^2 + 12603w - 35651 + 54976/w - 43884/w^2 + 14208/w^3, \quad (3)$$

where t_{burst} is in Myr, $w = \log \text{EW}(\text{H}\beta)$ and $\text{EW}(\text{H}\beta)$ is in Å. We adopt this relation in our analysis. Eq. 3 does not take into account the contribution of old stellar populations in the underlying galaxy. The effect of an underlying galaxy on the $ICF(\text{He})$ was discussed by Izotov et al. (2013) who found it to be small for high-excitation H II regions with $\text{EW}(\text{H}\beta) \geq 150 \text{ Å}$. Since the relations for $Z = 0.001$, $Z = 0.004$, and $Z = 0.008$ are similar for $\text{EW}(\text{H}\beta) \gtrsim 100 \text{ Å}$, corresponding to $t_{\text{burst}} \lesssim 4$ Myr, we have adopted Eq. 3 for the entire range of oxygen abundances in our sample galaxies. We have also adopted $t_{\text{burst}} = 1$ Myr and 4 Myr, when the derived starburst age was < 1 Myr or > 4 Myr. For t_{burst} in the range of 1 – 4 Myr, we have linearly interpolated between the fits given by Izotov et al. (2013) to derive $ICF(\text{He})$ and to correct for the non-recombination contri-

bution to the intensities of the hydrogen lines $\text{H}\alpha$, $\text{H}\beta$, $\text{H}\gamma$, and $\text{H}\delta$.

3.3 Correction for the fraction of oxygen locked in dust grains

Finally, the oxygen abundance should be corrected for its fraction locked in dust grains. Izotov et al. (2006) found the Ne/O abundance ratio in low-metallicity emission-line galaxies to increase with increasing oxygen abundance. They interpreted this trend by a larger fraction of oxygen locked in dust grains in galaxies with higher O/H. Following Izotov et al. (2013), we use the relation

$$\Delta \left(\frac{\text{O}}{\text{H}} \right)_{\text{dust}} = 10^{0.088(12 + \log \text{O/H}) - 0.616} \quad (4)$$

to derive the fraction of oxygen confined in dust.

This oxygen abundance locked in dust is added to the oxygen abundance in the gaseous phase, as derived from the emission-line fluxes.

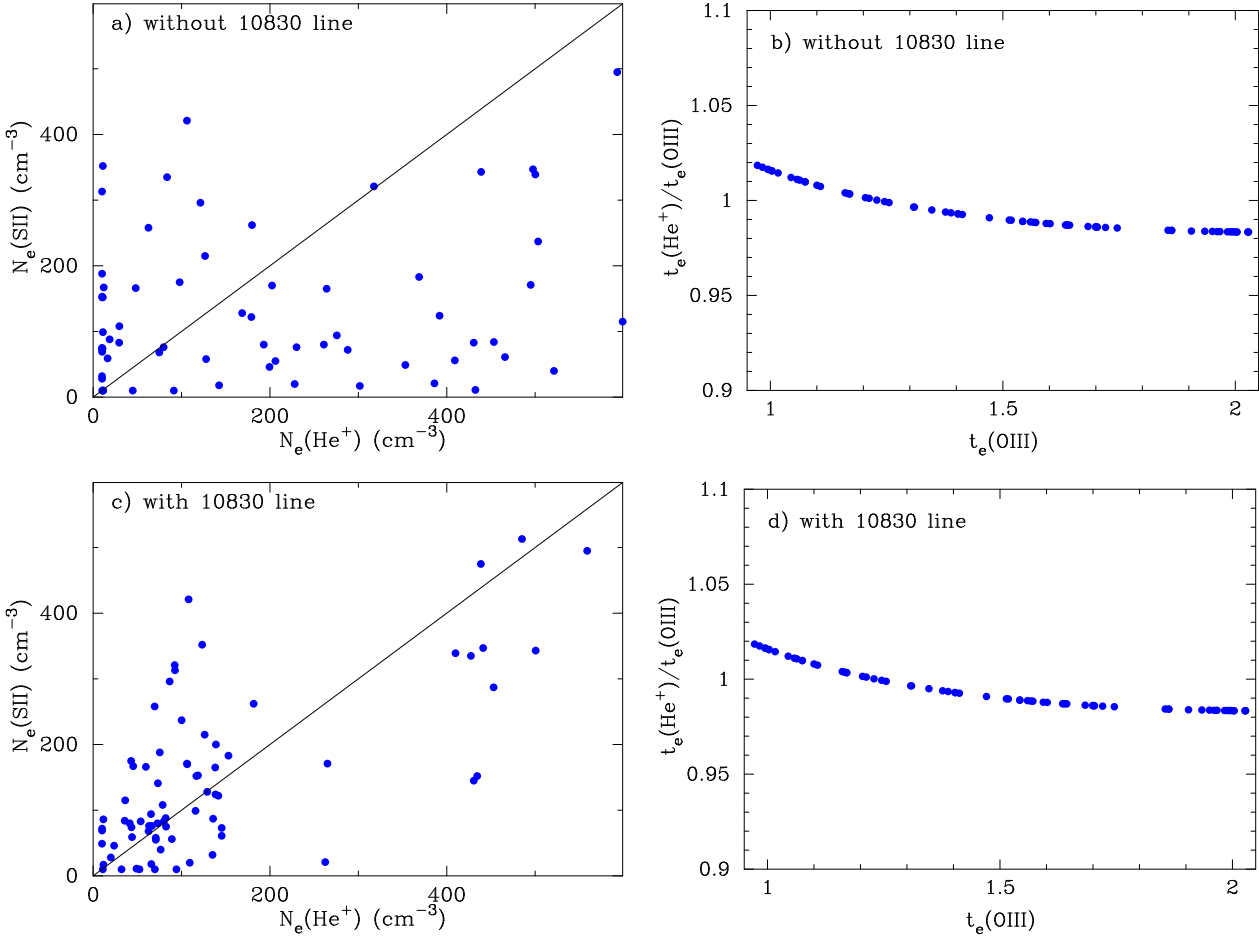


Figure 5. Same as in Fig. 4, but the electron temperature $T_e(\text{He}^+)$ is set equal to $\tilde{T}_e(\text{He}^+)$.

3.4 Monte Carlo method

To determine the He^+ abundance $y_i^+ = \text{He}_i^+/\text{H}^+$, we have applied the Monte Carlo procedure described in Izotov & Thuan (2004) and Izotov et al. (2007). We randomly vary the electron temperature $T_e(\text{He}^+)$, the electron number density $N_e(\text{He}^+)$ and the optical depth $\tau(\lambda 3889)$ within a specified range, to minimise the quantity

$$\chi^2 = \sum_i \frac{(y_i^+ - y_{\text{wm}}^+)^2}{\sigma^2(y_i^+)}. \quad (5)$$

The weighted mean of the y_i^+ , y_{wm}^+ , is defined by

$$y_{\text{wm}}^+ = \frac{\sum_i y_i^+ / \sigma^2(y_i^+)}{\sum_i 1 / \sigma^2(y_i^+)}, \quad (6)$$

where y_i^+ is the He^+ abundance derived from the intensity of the He I emission line labelled i , and $\sigma(y_i^+)$ is the statistical error of y_i^+ . Each y_i^+ has been assigned a weight inversely proportional to that statistical error, since fluxes of weaker emission lines are more uncertain and therefore should be attributed lower weights. The resulting y_{wm}^+ is the empirically derived He^+ abundance in each model.

Additionally, in the case of the nebular He II $\lambda 4686$ emission line, we have added the abundance of doubly ionised helium $y^{2+} \equiv \text{He}^{2+}/\text{H}^+$ to y^+ to calculate y . Although the He^{2+} zone is hotter than the He^+ zone, we have

adopted $T_e(\text{He}^{2+}) = T_e(\text{He}^+)$. The last assumption has only a minor effect on the y value, because except in a few high-excitation H II regions, y^{2+} is in general small ($\leq 1\%$ of y^+).

The total He abundance y is obtained from the expression $y = ICF(\text{He}) \times (y^+ + y^{2+})$, where $ICF(\text{He}) = \text{H}^+ / (\text{He}^+ + \text{He}^{2+})$ is the ionisation correction factor for He. It is converted to the He mass fraction using equation

$$Y = \frac{4y(1 - Z)}{1 + 4y}, \quad (7)$$

where $Z = B \times \text{O}/\text{H}$ is the heavy-element mass fraction. The coefficient B depends on O/Z , where O is the oxygen mass fraction. Maeder (1992) derived $\text{O}/Z = 0.66$ and 0.41 for $Z = 0.001$ and 0.02 , respectively. The latter value is close to the most recent determination for the Sun (0.43 , using the abundances of Asplund et al. 2009). Adopting the Maeder (1992) values, Izotov et al. (2013) obtained $B = 18.2$ and 27.7 for $Z = 0.001$ and 0.02 , respectively. B values are then assumed to linearly scale with the oxygen abundance $A(\text{O}) (= 12 + \log \text{O}/\text{H})$ according to the relation

$$B = 8.64A(\text{O}) - 47.44. \quad (8)$$

We adopt this relation in our calculations.

We varied $N_e(\text{He}^+)$ in the range $10 - 600 \text{ cm}^{-3}$. The electron temperature $T_e(\text{O III})$ was derived from the $[\text{O III}]\lambda 4363/(\lambda 4959 + \lambda 5007)$ emission line intensity ratio,

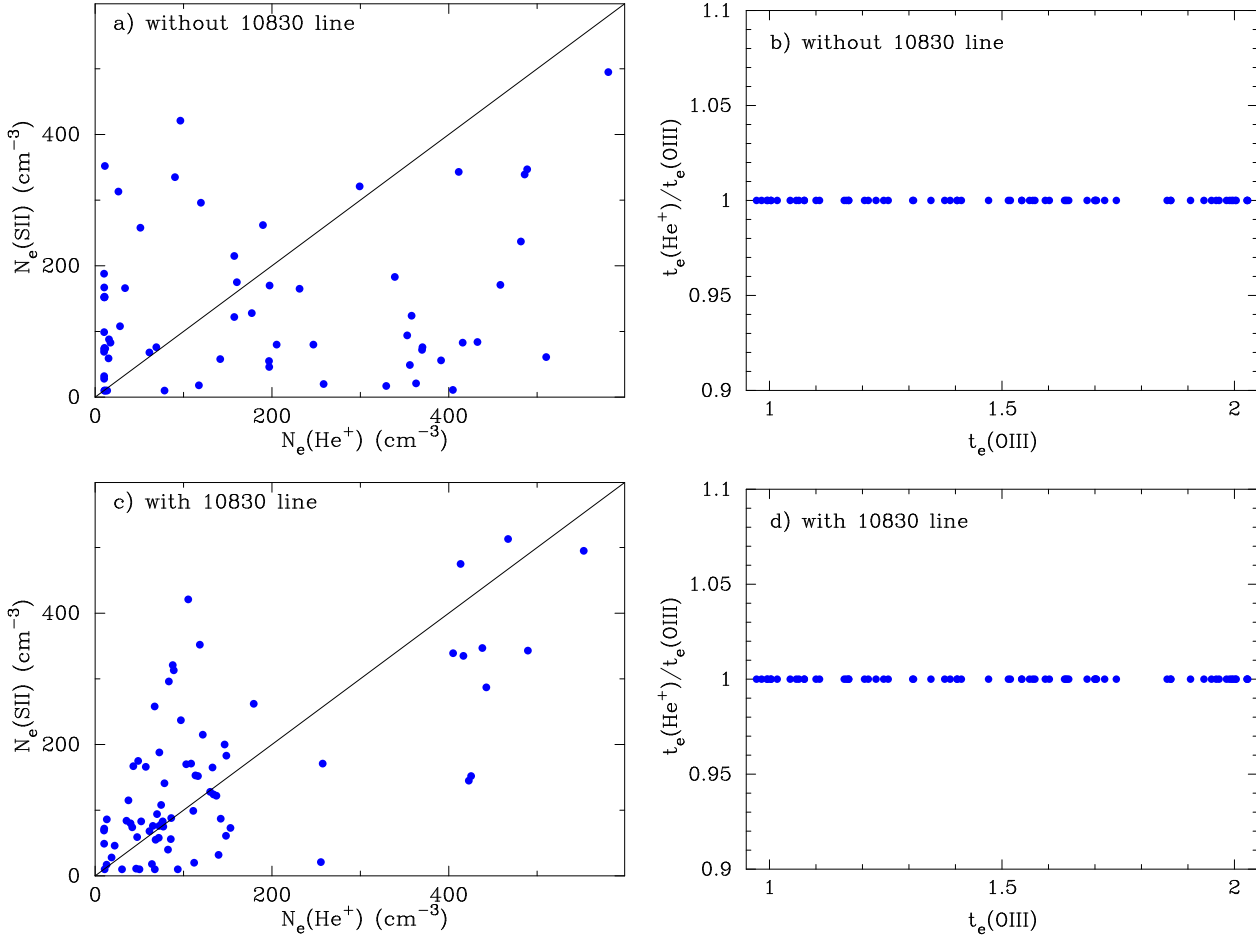


Figure 6. Same as in Fig. 4, but the electron temperature $T_e(\text{He}^+)$ is set equal to $T_e(\text{O III})$.

prior to determining Y . Izotov et al. (2013) showed that it is very close to the volume-emissivity-averaged value of the electron temperature in the O^{2+} zone calculated with CLOUDY grid models for the whole range of metallicities. For variations of the electron temperature $T_e(\text{He}^+)$, we have followed the prescriptions of Izotov et al. (2013). $T_e(\text{He}^+)$ was set in the three following ways:

1) $T_e(\text{He}^+)$ was randomly varied in the range (0.95 – 1.05) of the temperature derived from the relation between volume-averaged temperatures $T_e(\text{He}^+)$ and $T_e(\text{O III})$ in CLOUDY models, which Izotov et al. (2013) fitted by the expression

$$\tilde{T}_e(\text{He}^+) = 2.51 \times 10^{-6} T_e(\text{O III}) + 0.8756 + 1152/T_e(\text{O III}). \quad (9)$$

This relation predicts $\tilde{T}_e(\text{He}^+) < T_e(\text{O III})$ for hotter H II regions and $\tilde{T}_e(\text{He}^+) > T_e(\text{O III})$ for cooler H II regions;

2) $T_e(\text{He}^+) = \tilde{T}_e(\text{He}^+)$;

and

3) $T_e(\text{He}^+) = T_e(\text{O III})$.

As for the optical depth $\tau(\lambda 3889)$, we varied it randomly in the range 0 – 5.

3.5 The role of the He I $\lambda 10830\text{\AA}$ NIR line in the primordial helium abundance determination

We derive the He^+ abundance $y_i^+ = \text{He}_i^+/\text{H}^+$ using the strongest He I emission lines that are available. We consider two cases : 1) the case where all six strongest helium emission lines are used: the five $\lambda 3889$, $\lambda 4471$, $\lambda 5876$, $\lambda 6678$, $\lambda 7065$ optical lines and the NIR He I $\lambda 10830\text{\AA}$ line; 2) the case which makes use only of the five strongest optical helium emission lines, excluding the NIR He I $\lambda 10830\text{\AA}$ line. The latter case is the one we have considered in the past in all our previous work on the determination of the primordial helium abundance (Izotov & Thuan 2010; Izotov et al. 2013, and references therein). Comparing the two cases will allow us to assess the impact of the use of the NIR line on helium abundance determinations.

3.5.1 A small dispersion about the mean helium abundance

In Fig. 3, we show for the whole sample the ratios of Y s derived from individual lines to the weighted mean Y_{wm} as a function of oxygen abundance O/H . The sample consists of 75 optical spectra and 45 NIR spectra in 45 H II regions of 43 galaxies. The number of optical spectra is greater than that of NIR spectra, because some H II regions were observed several times in the optical range. All six lines were used in

the χ^2 minimisation and determination of Y_{wm} . It is seen that, for all lines, the Y_i/Y_{wm} values scatter around 1 (indicated by a horizontal line in each panel), as should be the case. However, the dispersions of the points about the value 1 are quite different, depending on the emission line. The He I $\lambda 10830\text{\AA}$ emission line, the one with the highest intensity, shows the smallest dispersion (panel f). On the other hand, the two He I $\lambda 3889\text{\AA}$ and He I $\lambda 7065\text{\AA}$ lines (panels a and e) show the highest dispersions. There are reasons for these high dispersions: the former line is blended with the H8 hydrogen line and the determination of its flux is subject to large uncertainties, while the latter line is generally the weakest of all six lines. This is the first virtue of the He I $\lambda 10830\text{\AA}$ NIR line: it plays a very important role in the determination of the helium abundance. Because of its very small dispersion about the weighted mean Y_{wm} , the latter quantity is determined to a large extent by this line.

3.5.2 Sensitivity to the electron density

We compare here the derived electron densities and temperatures of the He^+ zone compared to those derived for the S^+ and O^{2+} regions, respectively.

In Fig. 4a and 4b we show respectively the relations $N_e(\text{S II}) - N_e(\text{He}^+)$ and $T_e(\text{He}^+)/T_e(\text{O III}) - T_e(\text{O III})$, in the case where He I $\lambda 10830\text{\AA}$ is not used in the minimisation of χ^2 (Eq. 5) and the determination of Y_{wm} . $T_e(\text{He}^+)$ has been randomly varied in the range $(0.95 - 1.05)\tilde{T}_e(\text{He}^+)$. In agreement with Izotov et al. (2013), we found no correlation between the number densities $N_e(\text{S II})$ and $N_e(\text{He}^+)$ (Fig. 4a). This lack of correlation also holds for the derived temperatures. The $T_e(\text{He}^+)/T_e(\text{O III})$ ratio does not scatter around the value $\tilde{T}_e/T_e(\text{O III})$, but tends to be at either the lower $(0.95 \times \tilde{T}_e/T_e(\text{O III}))$ or upper boundary $(1.05 \times \tilde{T}_e/T_e(\text{O III}))$ of the range adopted for temperature variations, with a few points in between (Fig. 4b).

We next examine the situation when the He I $\lambda 10830\text{\AA}$ emission line is included in the minimisation of χ^2 and the determination of Y_{wm} (Fig. 4c,d). The temperature's behavior remains about the same (Fig. 4d). Apparently, our data is not accurate enough to allow a more precise derivation of the temperature $T_e(\text{He}^+)$ within the adopted small range of $\pm 5\%$ around \tilde{T}_e . However, we note that the $T_e(\text{He}^+)/T_e(\text{O III})$ ratios do appear to be slightly more evenly distributed between the lower and upper boundaries, especially for H II regions with $T_e(\text{O III}) < 15000\text{K}$. For H II regions with $T_e(\text{O III}) > 18000\text{K}$, there are also points scattered between the two boundaries, although they are less in number as compared to the case when the He I $\lambda 10830\text{\AA}$ line is not included. These hot H II regions play an important role in the determination of Y_p as they are the ones with the lowest metallicities. Therefore, on statistical ground, the average $T_e(\text{He}^+)$ for our H II region sample is similar to \tilde{T}_e , which is what is desired. Of course, the range of temperature variations can be enlarged, but this is difficult to justify physically because photoionised H II region models (e.g., those produced with the CLOUDY code) show that the temperatures in H^+ and He^+ zones cannot differ by more than a few percent from the temperature derived from the $[\text{O III}]$ emission lines.

On the other hand, there is now a clear correlation be-

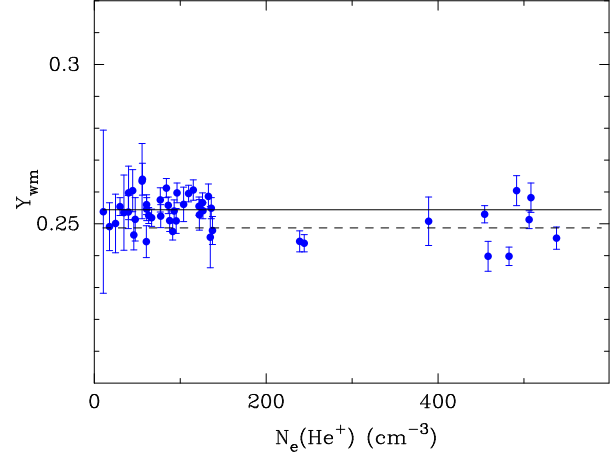


Figure 7. Relation between the derived number density $N_e(\text{He}^+)$ and helium mass fraction for low-metallicity H II regions, with $\text{O}/\text{H} \leq 10^{-4}$. All six He I emission lines $\lambda 3889$, $\lambda 4471$, $\lambda 5876$, $\lambda 6678$, $\lambda 7065$, and $\lambda 10830$ have been used for the χ^2 minimisation. The solid and dashed lines indicate the mean Y value for H II regions with $N_e(\text{He I}) \leq 200 \text{ cm}^{-3}$, and that for H II regions with $N_e(\text{He I}) > 200 \text{ cm}^{-3}$, respectively.

tween $N_e(\text{S II})$ and $N_e(\text{He}^+)$ (Fig. 4c), despite the relatively high dispersion. This is a consequence of the high sensitivity of the flux of the He I $\lambda 10830\text{\AA}$ line to the density of the H II region. The correlation between the number densities does not change appreciably when the electron temperature $T_e(\text{He}^+)$ is set to either $\tilde{T}_e(\text{He}^+)$ (Fig. 5) or $T_e(\text{O III})$ (Fig. 6).

Hence the second virtue of the He I $\lambda 10830\text{\AA}$ emission line is: the number density $N_e(\text{He}^+)$ is much better constrained when it is taken into account in the determination of helium abundances. We note, that temperature variations such as those shown in Figs. 4 – 6 do change the primordial helium mass fraction Y_p (considered in the next section), but only by a little amount, not exceeding 0.3%.

3.5.3 Density effects on the helium abundance

It is seen in Figs. 4c, 5c, and 6c that the number density $N_e(\text{He}^+)$ in several H II regions can be high, greater than 200 cm^{-3} . The near-infrared spectrum of one of those high-density H II regions is shown in Fig. 1a. It is characterised by a very high He I $\lambda 10830/\text{P}\gamma$ $\lambda 10940$ flux ratio (see also Table 2). Most of these high-density H II regions have low oxygen abundance $\text{O}/\text{H} < 10^{-4}$, corresponding to $12 + \log \text{O}/\text{H} < 8.0$. Some of them are among the lowest-metallicity galaxies known, with $12 + \log \text{O}/\text{H} \leq 7.6$. We check whether the helium mass fraction Y derived in the high-density H II regions differs from that in the low-density H II regions. In Fig. 7 we show the dependence of the weighted mean helium mass fraction Y_{wm} on the electron number density $N_e(\text{He}^+)$. Only low-metallicity galaxies, with $\text{O}/\text{H} < 10^{-4}$, are shown. We find that the average Y_{wm} in the high-density H II regions with $N_e(\text{He}^+) > 200 \text{ cm}^{-3}$ (dashed horizontal line) is $\gtrsim 2\%$ lower than that in the low-density H II regions with $N_e(\text{He}^+) < 200 \text{ cm}^{-3}$ (solid horizontal line).

Y_{wm} s are not expected to vary in H II regions with similar oxygen abundances, like those shown in Fig. 7. Yet, Fig. 7

shows that, in the mean, high-density H II regions have lower Y_{wm} than low-density H II regions. This is because the sensitivity of He I line fluxes to density is not the same for different lines. In fact, at a given density, collisional excitation effects for the He I $\lambda 10830\text{\AA}$ emission line are ~ 10 times stronger than for the He I $\lambda 5876\text{\AA}$ emission line. We have assumed in all our calculations that the density of the H II region is constant. However, this is not the case in reality. If some inhomogeneities and density gradients are present in the H II regions, then the observed volume-averaged fluxes of those He I lines that are more density-dependent would be more characteristic of the H II region denser parts than of its less dense parts. In particular, He I $\lambda 10830\text{\AA}$ is such a density-dependent line. It would tend to be more characteristic of the densest parts of an H II region. This would lead to an overcorrection for collisional excitation as compared to the case of a uniform H II region, and result in an underestimation of Y_{wm} . To avoid this effect, we will consider in our final sample only H II regions with an electron density $< 200 \text{ cm}^{-3}$. The choice of this cut-off is motivated by examination of Fig. 7 which tells us that the mean Y_{wm} of H II regions with densities greater than $\sim 200 \text{ cm}^{-3}$ is systematically lower than that for H II regions with $N_e(\text{He}^+) \lesssim 200 \text{ cm}^{-3}$. Furthermore, the flux of the He I $\lambda 10830\text{\AA}$ emission line due to collisional excitation in H II regions with $N_e(\text{He}^+) > 200 \text{ cm}^{-3}$ exceeds the recombination flux, indicating that this line is very sensitive to density inhomogeneities. On the other hand, the flux of the He I $\lambda 5876\text{\AA}$ emission line due to collisional excitation is at most only 10-20% of the total flux.

It is also possible that the difference in Y_{wm} is due to the uncertainties in the emissivities of the He I lines and their analytical fits. In particular, the analytical fits (see Fig. 1 in Izotov et al. 2013) at higher number densities deviate more from the exact values of emissivities than those at lower number densities (see also the discussion in Sect. 4.4).

4 PRIMORDIAL HE MASS FRACTION Y_p

As in our previous work (see Izotov et al. 2007, 2013; Izotov & Thuan 2010, and references therein), we determine the primordial He mass fraction Y_p by fitting the data points in the $Y - \text{O}/\text{H}$ plane with a linear regression line of the form (Peimbert & Torres-Peimbert 1974, 1976; Pagel et al. 1992)

$$Y = Y_p + \frac{dY}{d(\text{O}/\text{H})}(\text{O}/\text{H}). \quad (10)$$

To derive the parameters of the linear regressions, we used the maximum-likelihood method (Press et al. 1992), which takes into account the errors in Y and O/H for each object.

4.1 Inclusion of the He I $\lambda 10830\text{\AA}$ line

We consider linear regressions $Y - \text{O}/\text{H}$ for the entire sample, adopting an electron temperature $T_e(\text{He}^+)$ which is randomly varied in the range $(0.95 - 1.05)\tilde{T}_e(\text{He}^+)$ so as to minimise χ^2 , defined by Eq. 5. $\tilde{T}_e(\text{He}^+)$ is given by Eq. 9. We have performed regressions for both the case where He I $\lambda 10830\text{\AA}$ is not used in the determination of Y (Fig. 8a), and the case where that line is used (Fig. 8b). Comparison of Figs. 8a and

8b shows that the inclusion of the He I $\lambda 10830\text{\AA}$ emission line in the determination of Y_{wm} reduces the scatter of the points. The χ^2 per degree of freedom for the regression line in Fig. 8b is 4.02, while it is 5.48 in Fig. 8a. The $Y - \text{O}/\text{H}$ relation becomes tighter when high-density H II regions with $N_e(\text{H}^+) > 200 \text{ cm}^{-3}$ are excluded from the determination of Y_{wm} . With the exclusion of these H II regions, the χ^2 per degree of freedom becomes 2.38 (Fig. 9a).

Thus, the third virtue of the He I $\lambda 10830$ emission line is to make the $Y - \text{O}/\text{H}$ relation much tighter as compared to all previous studies.

4.2 Exclusion of the He I $\lambda 3889$ and $\lambda 7065$ lines and of high-density H II regions

The $Y - \text{O}/\text{H}$ relation becomes even tighter, with a χ^2 of only 1.12 (Fig. 9b), when the two most uncertain He I $\lambda 3889$ and $\lambda 7065$ emission lines (Fig. 2) are excluded from the determination of Y_{wm} . The He I $\lambda 3889$ line is uncertain because of contamination by the hydrogen H8 $\lambda 3889$ line, and the He I $\lambda 7065$ emission line is uncertain because of its weakness. The parameters derived for the sample shown in Fig. 9b, with the additional inclusion of the high-density H II regions, are presented in Table 3. The uncertainties of these parameters are propagated in the derivation of errors of the He mass fraction Y .

4.3 Final NIR sample

We have further restricted the final NIR sample to those H II regions with high $\text{EW}(\text{H}\beta)$ and high excitation parameters $x = \text{O}^{2+}/\text{O}$. Both these parameters are higher in younger starbursts. In their analysis of a large sample of several hundred galaxies, Izotov et al. (2013) have found that the weighted mean Y_{wm} increases with decreasing $\text{EW}(\text{H}\beta)$ and decreasing x (their Figs. 10a and 11). These trends are unphysical and suggest that objects with low $\text{EW}(\text{H}\beta)$ and low x should not be used for the determination of Y_p . The main reason for not including objects with low $\text{EW}(\text{H}\beta)$ is because of the larger contribution of the light of the underlying galaxy to their optical continuum, so that $\text{EW}(\text{H}\beta)$ is no longer an accurate starburst age indicator. The starburst age would then be overestimated, resulting in overestimated values of $\text{ICF}(\text{He})$ and Y_p . On the other hand, Izotov et al. (2013) have shown that no trend is apparent for galaxies with $\text{EW}(\text{H}\beta) \geq 150\text{\AA}$ and $x \geq 0.8$, limits which we adopt for our sample. Izotov et al. (2013) found that the $\text{ICF}(\text{He})$ derived for these galaxies using starburst ages based on $\text{EW}(\text{H}\beta)$ are consistent with those derived using SED fitting (their Fig. 12). There is a further advantage in using only high-excitation H II regions: He abundances for most objects with $\text{EW}(\text{H}\beta) \geq 150\text{\AA}$ and $x \geq 0.8$ are derived with an accuracy better than 3% because of a stronger $[\text{O III}] \lambda 4363$ emission, resulting in more accurate electron temperatures and derived abundances.

Therefore, our final sample (hereafter the NIR sample) consists only of those H II regions that have $\text{EW}(\text{H}\beta) \geq 150\text{\AA}$, excitation ratios $\text{O}^{2+}/\text{O} \geq 0.8$ and $\sigma(Y_{\text{wm}})/Y_{\text{wm}} \leq 3\%$. These selection criteria give a total sample of 28 H II regions. The linear regression for the NIR sample, excluding He I $\lambda 3889$ and $\lambda 7065$ from the determination of Y_{wm} , is

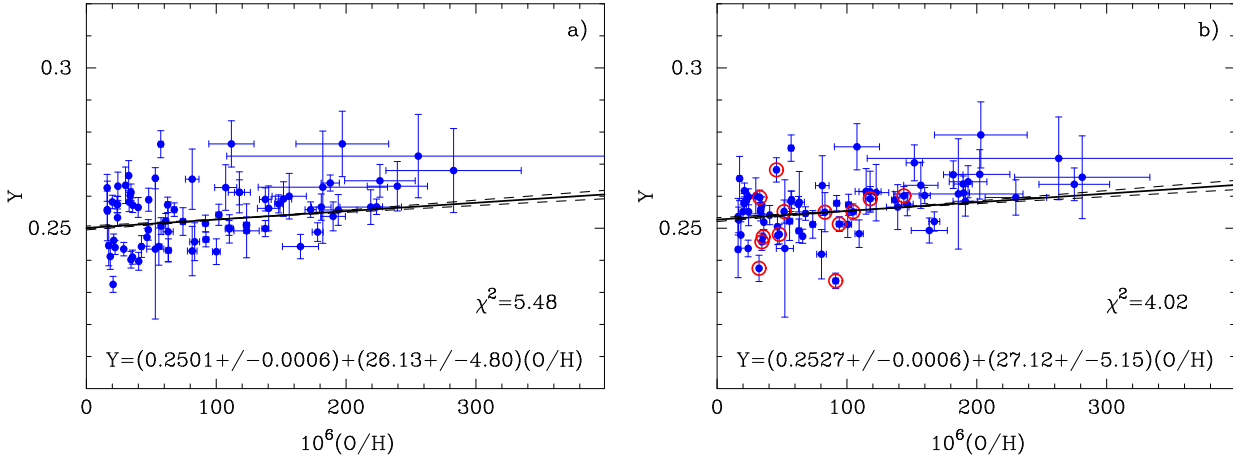


Figure 8. (a) $Y - O/H$ linear regression for the 75 spectra of 45 H II regions. Only the five He I optical emission lines $\lambda 3889$, $\lambda 4471$, $\lambda 5876$, $\lambda 6678$, and $\lambda 7065$ have been used for the χ^2 minimisation and determination of Y . $T_e(\text{He}^+)$ was varied in the range $0.95 - 1.05$ of the $\hat{T}_e(\text{He}^+)$ value. The equation of the linear regression and the value of the χ^2 are given at the bottom of each panel. (b) Same as (a), but all six He I emission lines $\lambda 3889$, $\lambda 4471$, $\lambda 5876$, $\lambda 6678$, $\lambda 7065$, and $\lambda 10830$ have been used for the χ^2 minimisation and determination of Y . The points representing high-density H II regions, with $N_e(\text{He}^+) > 200 \text{ cm}^{-3}$, are encircled in (b).

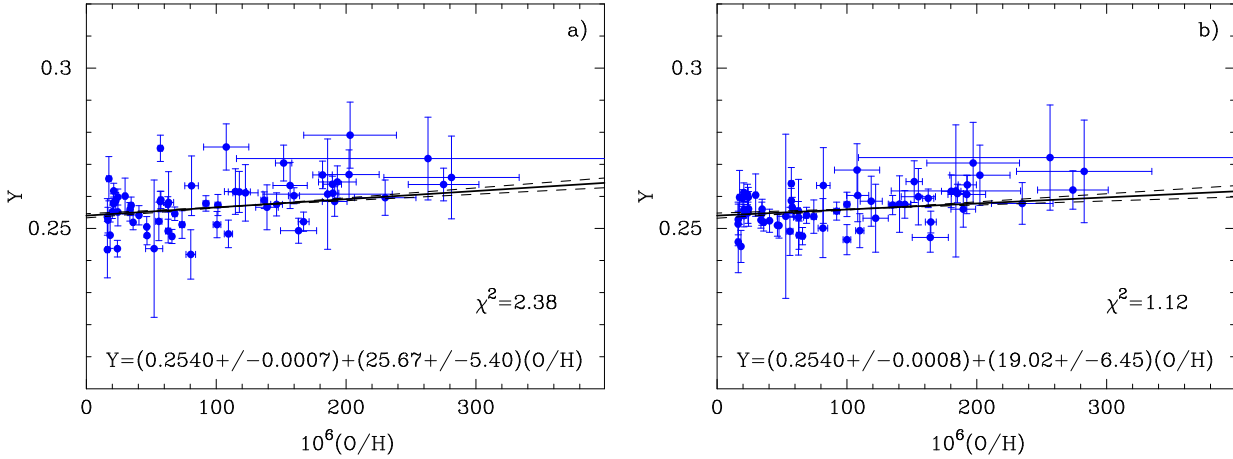


Figure 9. (a) Same as Fig. 8b, but high-density H II regions with $N_e(\text{He}^+) > 200 \text{ cm}^{-3}$ have been excluded. (b) Same as (a), but while all six He I emission lines $\lambda 3889$, $\lambda 4471$, $\lambda 5876$, $\lambda 6678$, $\lambda 7065$, and $\lambda 10830$ have been used for the χ^2 minimisation, only the four He I emission lines $\lambda 4471$, $\lambda 5876$, $\lambda 6678$, and $\lambda 10830$ have been used for the determination of Y .

shown in Fig. 10. We derive a primordial helium abundance mass fraction $Y_p = 0.2551 \pm 0.0010$ (statistical), with a χ^2 per degree of freedom of 1.43. Although the dispersion about the regression line is considerably smaller than that, for example, of the HeBCD sample analyzed by Izotov & Thuan (2010), the statistical error on the Y_p (0.0010) derived from the NIR sample is similar to the one derived for the HeBCD sample. This is because the size of the NIR sample (28 galaxies) is also considerably smaller than that of the HeBCD sample (86 galaxies).

For comparison, we have also derived Y_p for a sample where only the density limit has been set (i.e. the 13 H II regions with $N_e > 200 \text{ cm}^{-3}$ have been excluded), and where the conditions $x \geq 0.8$ and $\sigma(Y_{\text{wm}})/Y_{\text{wm}} \leq 3\%$ are not imposed (Fig. 9b). This results in a sample that is more than twice as large as the previous sample (62 instead of 28 H II regions), giving $Y_p = 0.2540 \pm 0.0008$, with a somewhat lower χ^2 of 1.12. This value is consistent, within a 1σ error, with the value $Y_p = 0.2551 \pm 0.0010$, obtained for the final sample.

We prefer however the final sample value as it is not subject to the unphysical trends discussed above.

4.4 Systematic effects

We now estimate the systematic errors in our helium abundance determination. We have considered three sources of systematic errors: 1) uncertainties of the He I emissivities and their fits; 2) uncertainties in the fits of the ionisation correction factors $ICF(\text{He})$; and 3) uncertainties due to the correction for the non-recombination contribution to hydrogen-line intensities.

Concerning the uncertainties in the He I emissivities, we used the results of Porter et al. (2009) who performed Monte Carlo calculations to estimate uncertainties of their old He I emissivities, not used here. They found that “optimistic” estimates of the uncertainties in the case of low-density extragalactic H II regions with $N_e = 100 \text{ cm}^{-3}$ are far below 1% for most of He I emission lines (Table 2 in Porter et al.

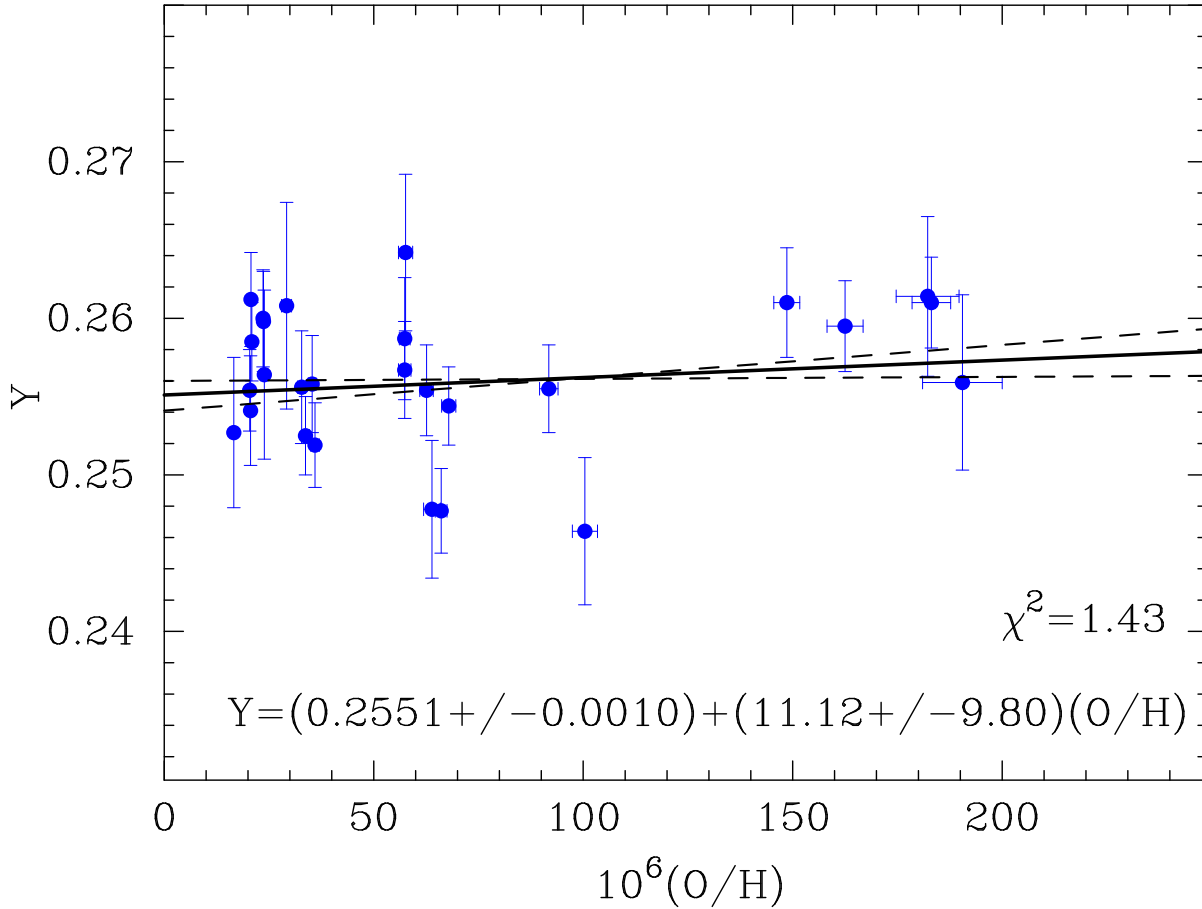


Figure 10. Same as in Fig. 8b, but only 28 H II regions with $\text{EW}(\text{H}\beta) \geq 150\text{\AA}$, an excitation parameter $\text{O}^{2+}/\text{O} \geq 0.8$ and a 1σ error in $Y \leq 3\%$ are included.

2009), except for the He I $\lambda 10830\text{\AA}$, for which the uncertainty can be as high as 2%. This gives a weighted emissivity uncertainty of less than 2% for all lines. Porter et al. (2009) also found the emissivity uncertainties to be higher in denser H II regions because of the uncertainties introduced by the collisional excitation parameters. They are thus ~ 5 - 10 times higher at $N_e = 10^4 \text{ cm}^{-3}$ than at $N_e = 10^2 \text{ cm}^{-3}$, the latter value approximating better the density of our H II regions. Porter et al. (2012) later analysed the uncertainties of the new emissivities that are used here, and found that the Porter et al. (2009) “optimistic” uncertainty estimates for the old emissivities become “realistic” estimates for the new ones.

Regarding the analytical fits of emissivities, they are accurate to better than 1% in the ranges $T_e = (1-2) \times 10^4 \text{ K}$ and $N_e \leq 100 \text{ cm}^{-3}$. Uncertainties increase however for denser H II regions (Fig. 1 in Izotov et al. 2013). Since the majority of our H II regions have low densities, we have adopted uncertainties of 1% for the He I emissivities and their fits.

As for the ionisation correction factors $ICF(\text{He})$, they do not deviate from unity by more than $\sim 2\%$ for all the H II regions in our sample (Table 3). That deviation depends on both the starburst age and the excitation parameter $x = \text{O}^{2+}/\text{O}$. From modeling photoionised H II regions with varying starburst ages and excitation parameters, Izotov et al. (2013) estimated the ICF uncertainties to be

$\sim 0.25\%$, which we adopt. Using the same photoionised H II region models Izotov et al. (2013) found a dispersion of 0.5% for the non-recombination intensities of hydrogen lines, varying starburst ages and metallicities (their Fig. 4). We thus adopt uncertainties of 0.5% for these quantities.

To estimate the systematic uncertainty introduced in Y_p by these effects, we have run Monte Carlo simulations varying the above three sources of systematic errors. We find that these uncertainty sources are responsible for a $\leq 0.75\%$ systematic error in Y_p , or 0.0019 in Y_p . Combining quadratically this systematic error with the statistical error of 0.0010 derived for the regression fit (Fig. 10), we obtain a total uncertainty of $\sqrt{0.0019^2 + 0.0010^2} = 0.0022$.

Thus, our final determination is:

$$Y_p = 0.2551 \pm 0.0022 \text{ (statistical + systematic)}. \quad (11)$$

The newly derived Y_p using the NIR He I line is in good agreement with the values derived by Izotov & Thuan (2010) and Aver et al. (2012). However, this agreement is somewhat fortuitous because different sets of He I emissivities and corrections for non-recombination excitation of hydrogen lines have been used in these various studies.

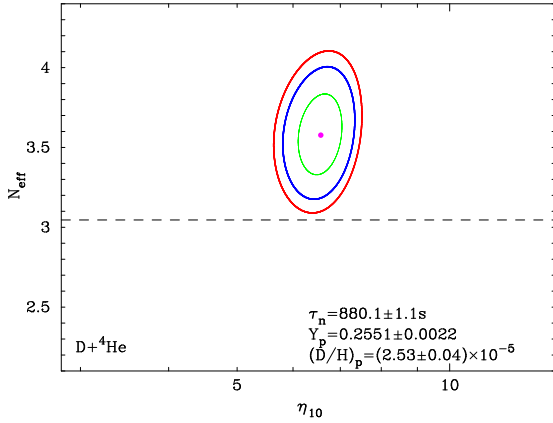


Figure 11. Joint fits to the baryon-to-photon number ratio, $\eta_{10}=10^{10}\eta$, and the effective number of light neutrino species N_{eff} , using a χ^2 analysis with the code developed by Fiorentini et al. (1998) and Lisi et al. (1999). The primordial value of the He abundance has been set to $Y_p = 0.2551$ (Fig. 9) and that of $(D/H)_p$ is taken from Cooke et al. (2014). The neutron lifetime is taken to be $\tau_n = 880.1 \pm 1.1$ s (Beringer et al. 2012). The filled circle corresponds to $\chi^2 = \chi^2_{\text{min}} = 0$. Ellipses from the inside out correspond respectively to confidence levels of 68.3% ($\chi^2 - \chi^2_{\text{min}} = 2.30$), 95.4% ($\chi^2 - \chi^2_{\text{min}} = 6.17$) and 99.0% ($\chi^2 - \chi^2_{\text{min}} = 9.21$). The SBBN value $N_{\text{eff}} = 3.046$ is shown with a dashed line.

5 COSMOLOGICAL IMPLICATIONS

The primordial He mass fraction we have derived is higher (at the 3.4σ level) than the SBBN value of 0.2477 ± 0.0001 inferred from analysis of the temperature fluctuations of the cosmic microwave background (CMB) radiation observed by the *Planck* satellite (Ade et al. 2013), in the context of the standard spatially flat six-parameter Λ CDM model. This may indicate small deviations from the standard rate of Hubble expansion in the early Universe. These deviations may be caused by an extra contribution to the total energy density of the Universe from a “dark radiation” component, for example, additional species of neutrinos such as “sterile” neutrinos (Di Valentino et al. 2013). The different species of weakly interacting light relativistic particles can be conveniently characterised by the parameter N_{eff} , the effective number of neutrino species.

We have used the statistical χ^2 technique, with the code described by Fiorentini et al. (1998) and Lisi et al. (1999), to analyse the constraints to the measured He and D abundances put on the baryon-to-photon number ratio η and N_{eff} . We have not included the abundance of ${}^7\text{Li}$ as a constraint because the discrepancy between the low lithium abundances measured in metal-poor halo stars in the Milky Way and the predictions of SBBN has not yet been resolved satisfactorily (Steigman 2012). We have adopted a deuterium abundance $(D/H)_p = (2.53 \pm 0.04) \times 10^{-5}$ (Cooke et al. 2014), and the most recently published value for the neutron lifetime $\tau_n = 880.1 \pm 1.1$ s (Beringer et al. 2012).

The joint fits of η and N_{eff} are shown in Figure 11. With two degrees of freedom (η_{10} and N_{eff}), deviations at the 68.3% confidence level (CL) correspond to $\chi^2 - \chi^2_{\text{min}} = 2.30$, those at the 95.4% CL to $\chi^2 - \chi^2_{\text{min}} = 6.17$, and those

at the 99.0% CL to $\chi^2 - \chi^2_{\text{min}} = 9.21$. These confidence levels are shown in Figure 11 by ellipses from the inside out.

With $Y_p = 0.2551 \pm 0.0022$, the minimum $\chi^2_{\text{min}} = 0$ is obtained for $\eta_{10} = 6.57$, corresponding to $\Omega_b h^2 = 0.0240 \pm 0.0017$ (68% CL), ± 0.0028 (95.4% CL) and ± 0.0034 (99.0% CL), and to $N_{\text{eff}} = 3.58 \pm 0.25$ (68% CL), ± 0.40 (95.4% CL) and ± 0.50 (99.0% CL). Our derived value of $\Omega_b h^2$ is in agreement, within the errors, with the ones derived from the WMAP-7 and Planck CMB data of respectively 0.0222 ± 0.0004 (Keisler et al. 2011) and 0.0221 ± 0.00033 (68% CL) (Ade et al. 2013).

However, our derived value of N_{eff} is higher than the SBBN value of 3.046 at the 99% CL, implying deviations from SBBN. We note that, while the primordial helium abundance is not as precise a baryometer as deuterium, it sets tight constraints on the effective number of neutrino species. These constraints are similar to or are tighter than those derived using the CMB and galaxy clustering power spectra. For example, using these two sets of data, Komatsu et al. (2011) derived $N_{\text{eff}} = 4.34^{+0.86}_{-0.88}$ at the 68% confidence level. Keisler et al. (2011) analysed joint WMAP-7 and South Pole Telescope (SPT) data on CMB temperature fluctuations derived $N_{\text{eff}} = 3.85 \pm 0.62$ (68% CL). Adding low-redshift measurements of the Hubble constant H_0 using the Hubble Space Telescope, and the baryon acoustic oscillations (BAO) using SDSS and 2dFGRS, Keisler et al. (2011) obtained $N_{\text{eff}} = 3.86 \pm 0.42$ (68% CL). On the other hand, Ade et al. (2013), using the data of the *Planck* mission, derived $N_{\text{eff}} = 3.30 \pm 0.27$ (68% CL), while Dvorkin et al. (2014) obtained $N_{\text{eff}} = 3.86 \pm 0.25$ by combining data from the *Planck* and ACT/SPT temperature spectra, WMAP-9 polarization, H_0 , baryon acoustic oscillation and local cluster abundance measurements with BICEP2 data. Thus, there appears to be general agreement between the N_{eff} obtained in this paper and the values derived by other researchers with different methods: a non-standard value is preferred at the 99% CL.

6 CONCLUSIONS

We present for the first time spectroscopic observations in the near-infrared (NIR) range of the high-intensity density-sensitive He I $\lambda 10830\text{\AA}$ emission line for a large sample of 45 low-metallicity high-excitation H II regions in star-forming dwarf galaxies. Using this NIR line flux in combination with existing spectroscopic data in the optical range of the same H II regions, we have obtained a new determination of the primordial He abundance. At the same time, we have also shown the importance of the He I NIR line for improving the accuracy of He abundance determinations.

Our main results are summarised below.

1. We demonstrate that the use of the He I $\lambda 10830\text{\AA}$ emission line greatly improves the determination of the physical conditions in the H II regions because of the strong dependence of its flux on the electron number density.

2. We find that the linear regressions $Y - \text{O}/\text{H}$ used for determination of the primordial He mass fraction Y_p are much tighter than those studied previously if the NIR He I $\lambda 10830\text{\AA}$ emission line is included, rather than relying only on the optical He I lines.

3. Using the linear regression $Y - \text{O}/\text{H}$ for a sample of 28 highest-excitation H II regions, we have derived a primor-

dial He mass fraction $Y_p = 0.2551 \pm 0.0022$. This is higher than the standard big bang nucleosynthesis (SBBN) value of 0.2477 ± 0.0001 inferred from the temperature fluctuations of the microwave background radiation. This difference possibly indicates deviations from the standard rate of Hubble expansion in the early Universe, and hence the possible presence of dark radiation.

4. Using our derived He primordial abundance together with the most recently derived primordial abundance of D, and the χ^2 technique, we found that the best agreement between the abundances of these light elements is achieved in the BBN model with a baryon mass fraction $\Omega_b h^2 = 0.0240 \pm 0.0034$ (99% CL) and an effective number of neutrino species $N_{\text{eff}} = 3.58 \pm 0.50$ (99% CL). Both the $\Omega_b h^2$ and N_{eff} values agree with those inferred from the temperature fluctuations of the microwave background radiation. A non-standard value of N_{eff} is preferred at the 99% CL, implying the possible existence of additional types of neutrino species.

ACKNOWLEDGMENTS

Y.I.I. thanks the University of Virginia for warm hospitality. T.X.T. acknowledges the financial support of NASA/JPL grant RSA1463350. This study is based on observations made with ESO Telescopes at the La Silla Paranal Observatory under programmes 59.A-9004(D), 64.H-0467(A), 65.I-0097(A), and 67.B-0287(B). It is also based on observations with the Large Binocular Telescope (LBT) and the Apache Point Observatory (APO) 3.5m telescope. The LBT is an international collaboration among institutions in the United States, Italy and Germany. LBT Corporation partners are: The University of Arizona on behalf of the Arizona university system; Istituto Nazionale di Astrofisica, Italy; LBT Beteiligungsgesellschaft, Germany, representing the Max-Planck Society, the Astrophysical Institute Potsdam, and Heidelberg University; The Ohio State University, and The Research Corporation, on behalf of The University of Notre Dame, University of Minnesota and University of Virginia. The APO 3.5m telescope is owned and operated by the Astrophysical Research Consortium. Funding for the Sloan Digital Sky Survey (SDSS) and SDSS-II has been provided by the Alfred P. Sloan Foundation, the Participating Institutions, the National Science Foundation, the U.S. Department of Energy, the National Aeronautics and Space Administration, the Japanese Monbukagakusho, the Max Planck Society, and the Higher Education Funding Council for England.

REFERENCES

- Abazajian, K., et al. 2009, *ApJS*, 182, 543
 Planck Collaboration: Ade, P. A. R., et al. 2013, *A&A*, in press; preprint arXiv:1303.5076
 Asplund, M., Grevesse, N., & Sauval, A. J. & Scott, P. 2009, *ARAA*, 47, 481
 Aver, E., Olive, K. A., & Skillman, E. D. 2010, *J. Cosmology Astropart. Phys.*, 05, 003A
 Aver, E., Olive, K. A., & Skillman, E. D. 2011, *J. Cosmology Astropart. Phys.*, 03, 043A
 Aver, E., Olive, K. A., & Skillman, E. D. 2012, *J. Cosmology Astropart. Phys.*, 04, 004A
 Aver, E., Olive, K. A., Porter, R. L., & Skillman, E. D. 2013, *J. Cosmology Astropart. Phys.*, 11, 017A
 Benjamin, R. A., Skillman, E. D., & Smits, D. P. 1999, *ApJ*, 514, 307
 Benjamin, R. A., Skillman, E. D., & Smits, D. P. 2002, *ApJ*, 569, 288
 Beringer, J., et al. (Particle Data Group) 2012, *Phys. Rev. D*, 86, 010001
 Cardelli, J. A., Clayton, G. C., & Mathis, J. S. 1989, *ApJ*, 345, 245
 Cooke, R. J., Pettini, M., Jorgenson, R. A., Murphy, M. T., & Steidel, C. C. 2014, *ApJ*, 781, 31
 Di Valentino, E., Melchiorri, A., & Mena, O. 2013, *J. Cosmology Astropart. Phys.*, 11, 018D
 Dvorkin, C., Wyman, M., Rudd, D. H., & Hu, W. 2014, preprint arXiv:1403.8049
 Ferland, G. J., Korista, K. T., Verner, D. A., Ferguson, J. W., Kingdon, J. B., & Verner, E. M. 1998, *PASP*, 110, 761
 Ferland, G. J., et al. 2013, *Rev. Mexicana Astron. Astrofis.*, 49, 137
 Fiorentini, G., Lisi, E., Sarkar, S., & Villante, F. L. 1998, *Phys. Rev. D*, 58, 063506
 González Delgado, R. M., Cerviño, M., Martins, L. P., Leitherer, C., & Hauschildt, P. H. 2005, *MNRAS*, 357, 945
 Guseva, N. G., Papaderos, P., Izotov, Y. I., Green, R. F., Fricke, K. J., Thuan, T. X., & Noeske, K. G. 2003, *A&A*, 2003, 407, 105
 Guseva, N. G., Izotov, Y. I., Stasińska, G., Fricke, K. J., Henkel, C., & Papaderos, P. 2011, *A&A*, 529, A149
 Hummer, D. G., & Storey, P. J. 1992, *MNRAS*, 254, 277
 Iocco, F., Mangano, G., Miele, G., Pisanti, O., & Serpico, P. D. 2009, *Phys.Rept.*, 472, 1
 Izotov, Y. I., & Thuan, T. X. 1998, *ApJ*, 500, 188
 Izotov, Y. I., & Thuan, T. X. 2004, *ApJ*, 602, 200
 Izotov, Y. I., & Thuan, T. X. 2010, *ApJ*, 710, L67
 Izotov, Y. I., Thuan, T. X., & Lipovetsky, V. A. 1994, *ApJ*, 435, 647
 Izotov, Y. I., Thuan, T. X., & Lipovetsky, V. A. 1997, *ApJS*, 108, 1
 Izotov, Y. I., Chaffee, F. H., Foltz, C. B., Green, R. F., Guseva, N. G., & Thuan, T. X. 1999, *ApJ*, 527, 757
 Izotov, Y. I., Chaffee, F. H., & Green, R. F. 2001, *ApJ*, 562, 727
 Izotov, Y. I., Papaderos, P., Guseva, N. G., Fricke, K. J., & Thuan, T. X. 2004, *A&A*, 421, 539
 Izotov, Y. I., Stasińska, G., Meynet, G., Guseva, N. G., & Thuan, T. X. 2006, *A&A*, 448, 955
 Izotov, Y. I., Thuan, T. X., & Stasińska, G. 2007, *ApJ*, 662, 15
 Izotov, Y. I., Guseva, N. G., Fricke, K. J., & Papaderos, P. 2009, *A&A*, 503, 61
 Izotov, Y. I., Guseva, N. G., Fricke, K. J., & Henkel, C. 2011, *A&A*, 533, A25
 Izotov, Y. I., Stasiska, G., & Guseva, N. G. 2013, *A&A*, 558, A57
 Keisler, R., Reichardt C. L., Aird, K. A., et al. 2011, *ApJ*, 743, 28
 Komatsu, E., et al. 2011, *ApJS*, 192, 18
 Leitherer, C., Schaerer, D., Goldader, J. D., Gonzalez Del-

- gado, R. M., Robert, C., Kune D. F., de Mello, D. F., Devost, D., & Heckman, T. M. 1999, *ApJS*, 123, 3
- Lisi, E., Sarkar, S., & Villante, F. L. 1999, *Phys. Rev. D*, 59, 123520
- Maeder, A. 1992, *A&A*, 264, 105
- Noterdaeme, P., López, S., Dumont, V., Ledoux, C., Molaro, P., & Petitjean, P. 2012, *A&A*, 542, L33
- Pagel, B. E. J., Simonson, E. A., Terlevich, R. J., & Edmunds, M. G. 1992, *MNRAS*, 255, 325
- Peimbert, M., & Torres-Peimbert, S. 1974, *ApJ*, 193, 327
- Peimbert, M., & Torres-Peimbert, S. 1976, *ApJ*, 203, 581
- Peimbert, M., Luridiana, V., & Peimbert, A. 2007, *ApJ*, 666, 636
- Pettini, M., & Cooke, R. 2012, *MNRAS*, 425, 2477
- Porter, R. L., Ferland, G. J., MacAdam, K. B., & Storey, P. J. 2009, *MNRAS*, 393, L36
- Porter, R. L., Ferland, G. J., Storey, P. J., & Detisch, M. J. 2012, *MNRAS*, 425, L28
- Porter, R. L., Ferland, G. J., Storey, P. J., & Detisch, M. J. 2013, *MNRAS*, 433, L89
- Press, W. H., Teukolsky, S. A., Vetterling, W. T., & Flannery, B. P., 1992, *Numerical Recipes in C, The Art of Scientific Computing /Second Edition/*, Cambridge University Press
- Steigman, G. 2005, *Phys. Scr.*, T121, 142
- Steigman, G. 2006, *Int. J. Mod. Phys. E*, 15, 1
- Steigman, G. 2012, preprint arXiv:1208.0032
- Wilson, J. C., et al. 2004, *Proc. SPIE*, 5492, 1295

This paper has been typeset from a \LaTeX file prepared by the author.